Slender body theory for ultrathin plates in two-dimensional viscous flow

Giulia Salussolia [*,†]
School of Engineering, Faculty of Science, Engineering and Technology, Universidad Mayor, Santiago 7500994, Chile

Catherine Kamal [‡]
Department of Mathematics, University College London, London WC1H 0AY, United Kingdom

(Received 18 November 2024; accepted 31 March 2025; published 7 May 2025)

The numerical modeling of ultrathin platelike particles in viscous flow is challenging because it requires an accurate representation of the particles' ultrathin edge. However, in many flow conditions, the effect of the edges on the flow and rheology is negligible. This paper presents a slender body theory for active or passive platelike particles in two-dimensional viscous flow. The theory simplifies the treatment of the particle geometry for the fluid-structure interaction, particularly by excluding the edge effects. The slender body theory is derived from the boundary integral formulation of the incompressible Stokes equations, which recasts the equations as an integral equation over the boundary of the particle's cross-section. By expanding the integral equation to leading order via a matched asymptotic expansion in the particle slenderness, a simplified nonlocal line integral across the central line of the particle is obtained. This integral relates the flow velocity and the hydrodynamic traction and does not depend on nontrivial edge effects. The results are validated for passive and active cases of ultrathin two-dimensional particles for which analytical results are known. The validations confirm the capability of the two-dimensional slender body theory to accurately describe the flow and rheology of passive and active ultrathin platelike particles under many flow conditions.

DOI: 10.1103/PhysRevFluids.10.054301

I. INTRODUCTION

From the transport of clay particles in rivers [1] to the flow and rheology of graphene suspensions for nano-ink-jet printing of deformable electric devices [2,3], predicting the motion of ultrathin platelike particles in viscous flow is crucial in the field of colloidal science. However, their irregular slender shape can pose significant computational challenges for fluid-structure modeling (see, for example, Ref. [4]). Specifically, the accurate representation of the particles' ultrathin edges can lead to computationally expensive simulations, especially when dealing with high particle concentrations or extremely small geometric aspect ratios [5]. To mitigate these challenges, platelike particles are often simulated in a two-dimensional flow domain [6–8]. Nonetheless, even the modeling of two-dimensional flow domains can become expensive for a relatively small number of particles. For example, boundary integral simulations of two-dimensional particles require iterative numerical methods for periodic systems with as few as 32 particles in [6–8]. There is a need to simplify

[*]Contact author: giulia.salussolia@umayor.cl
[†]Also at Multidisciplinary Center for Physics, Vicerrectoría de Investigación, Universidad Mayor, Santiago 8580745, Chile.
[‡]Contact author: c.kamal@ucl.ac.uk

the model at the base of the problem, particularly concerning the fluid-structure interaction of the plate.

This paper aims to create a nonlocal slender body theory (SBT) to compute the fluid-structure interaction of two-dimensional (2D) particles in viscous flow, for situations in which the edge effects are negligible. Slender body theory was first developed to model the flow dynamics of passive and active filaments. The underlying idea is to take advantage of the particle's slender structure to formulate a simplified model for the fluid-particle interaction. In the filament case, the fluid-structure interaction is reduced to a nonlocal one-dimensional line integral, which relates the velocity of the flow field and/or filament to the distributed hydrodynamic traction acting on the filament's surface [9–11]. This method has also been used to derive a nonlocal SBT for particles with a ribbon [12] or tubular [13] shape.

Despite the wide use and success of slender body theory for the upscale modeling of active and passive filaments in flow (e.g., [14,15]), the counterpart of this theory for ultrathin platelike particles is currently lacking. Alternative coarse-grain approaches have been used to simulate plates in a three-dimensional domain. For these cases, the particles are modeled via particle-laden methods such as Stokesian dynamics [16], variations of Stokesian dynamics whereby the particle is modeled as an assembly of spheres [17,18], or a coupled lattice Boltzmann and discrete element method [19]. However, these methods become too computationally costly for ultrathin particles. On the other hand, molecular-dynamics simulations of elastic plates have proved effective in describing flexible platelike particles [20]. Nonetheless, these simulations are computationally too expensive when dealing with ultrathin particles or platelike particles on a lengthscale qualitatively similar to those used in real-life applications. Molecular-dynamics simulations are also restrictive to computing suspensions with a sufficiently large number of these particles [20].

Recently, a nonlocal approximation of the fluid-structure interaction of elastic platelike particles has been suggested in a three-dimensional fluid domain [21,22] and in a two-dimensional fluid domain [23–25]. The approximation relies on using a nonlocal distribution of point forces over the major cross-section of the particle, instead of resolving the traction distribution on the whole surface. However, a rigorous justification of the model's assumptions and capability in viscous flow is currently missing.

In the boundary integral formulation for a two-dimensional flow domain, the two-dimensional incompressible Stokes equations are represented as an integral equation over the boundary of the particle's cross-section. Our approach to obtain the two-dimensional SBT model (which we refer to as 2D SBT) consists in expanding the two-dimensional boundary integral via a matched asymptotic expansion to leading order in the particle's slenderness [12]. With this derivation, we obtain a nonlocal 2D SBT formulation for the boundary's hydrodynamic traction and fluid's velocity on the centerline of the particle instead of its boundary. In our model, we give the 2D SBT equations up to leading order in the particle's slenderness. At higher order, the nontrivial edge stresses become significant. Modeling the edge stresses requires a computational resolution that accounts for an accurate representation of the edges, which is contrary to the model's objective of reducing the computational cost. Finally, we verify our formulation by using the 2D SBT model to compute (i) the motion of a two-dimensional circular arc in an external shear flow field [26], (ii) the orientational-dependent stresslet tensor for an ultrathin platelike particle in an external two-dimensional shear flow field [8], and (iii) the propagating speed of a two-dimensional swimming sheet at low Reynolds number (Taylor's sheet) [27,28]. For these cases, the 2D SBT computations are compared directly to existing analytical theory.

The outline of this article is as follows. In Sec. II, the derivation of a nonlocal 2D SBT for ultrathin platelike particles in two-dimensional viscous flow is presented. In Sec. III, the complete 2D SBT model is given, together with guidelines and simplifications. In Secs. IV, V, and VI, the 2D SBT theory is validated against the aforementioned analytical solutions (two-dimensional circular arcs in an external shear flow field, stresslet tensor for a flat plate in an external shear flow field, and average swimming speed of a Taylor sheet).

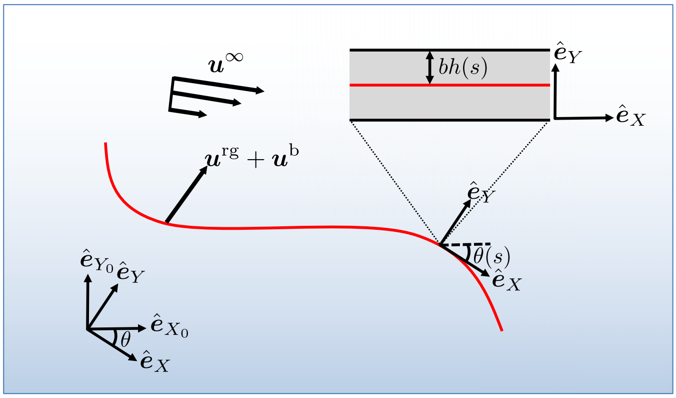

FIG. 1. Sketch of a slender two-dimensional body in an external flow field.

II. SBT FOR A TWO-DIMENSIONAL PLATE: FORMULATION

A. Boundary integral formulation

We use the two-dimensional boundary integral method to derive a slender body theory (2D SBT) for an ultrathin platelike particle immersed in a two-dimensional viscous flow field $\boldsymbol{u}^\infty$. The particle has infinite depth in the $\hat{\boldsymbol{e}}_z$ direction. We assume that this direction is perpendicular to the plane of flow $\boldsymbol{u}^\infty$ so that the problem is effectively two-dimensional. We parametrize the particle using the arc-length s running through the particle's longitudinal center. The particle surface is parametrized about the frame of reference attached to the center of the particle $(\hat{\boldsymbol{e}}_{X_0}, \hat{\boldsymbol{e}}_{Y_0})$, which corresponds to the position where $s = 0$. In this frame of reference, the closed boundary of the particle's cross-section is parametrized as $S = \{(aX_0(s) \pm bh(s)\sin\theta(s), aY_0(s) \pm bh(s)\cos\theta(s)) : -1 \leqslant s \leqslant 1\}$. Here, $\boldsymbol{x}_0(s) = a(X_0(s), Y_0(s))$ is the centerline of the particle, a is the particle's half-length, $bh(s)$ is the half-thickness of the particle (in the direction normal to the centerline and with maximum half-thickness b), and $\theta(s)$ is the clockwise angle taken from $\hat{\boldsymbol{e}}_{X_0}$ to the tangent of the centerline $\boldsymbol{x}_0(s)$ as shown in Fig. 1. We assume that the particle is ultrathin, which corresponds to a geometric aspect ratio $k = b/a \ll 1$. The unit vectors $\hat{\boldsymbol{e}}_X$ and $\hat{\boldsymbol{e}}_Y$ denote the unit-direction tangent and normal to the centerline of the particle, respectively, defined as

$$\hat{\boldsymbol{e}}_Y = \cos\theta\hat{\boldsymbol{e}}_{Y_0} + \sin\theta\hat{\boldsymbol{e}}_{X_0}, \quad \hat{\boldsymbol{e}}_X = -\sin\theta\hat{\boldsymbol{e}}_{Y_0} + \cos\theta\hat{\boldsymbol{e}}_{X_0}. \tag{1}$$

Note that in most of our equations, we drop the parametrization index "$[\cdot](s)$" for simplicity. The centerline $\boldsymbol{x}_0$ can be expressed using curvilinear coordinates as

$$Y_0' = -\sin\theta, \quad X_0' = \cos\theta, \quad \theta' = \kappa. \tag{2}$$

The prime $[\cdot]'$ denotes the derivative with respect to s, and κ is the curvature of the centerline.

The flow field $\boldsymbol{u}$ (given by the sum of the undisturbed flow $\boldsymbol{u}^\infty$ and the particle disturbance), the ambient pressure field p_a, and the associated stress tensor $\boldsymbol{\sigma}$ are assumed to satisfy the incompressible Stokes equations,

$$\nabla\cdot\boldsymbol{\sigma} = \boldsymbol{0}, \quad \sigma_{ij} = -\delta_{ij}p_a + \eta\left(\frac{\partial u_i}{\partial x_j} + \frac{\partial u_j}{\partial x_i}\right), \quad \nabla\cdot\boldsymbol{u} = \boldsymbol{0}. \tag{3}$$

Here, η is the viscosity of the fluid.

The boundary integral equation provides a closed expression for the traction $\boldsymbol{f} = \boldsymbol{\sigma}\cdot\boldsymbol{n}$ (where $\boldsymbol{n}$ is the surface normal pointing into the fluid) over the surface of a body moving with velocity $\boldsymbol{u}^{rg} + \boldsymbol{u}^b$. Here $\boldsymbol{u}^{rg}$ is the rigid body motion of the particle, defined as $\boldsymbol{u}^{rg} = \Omega\hat{\boldsymbol{e}}_z \times \boldsymbol{x} + \boldsymbol{U}$ for angular velocity Ω and translation velocity $\boldsymbol{U}$, and $\boldsymbol{u}^b$ is the velocity corresponding to the dynamic change in shape of the particle's centerline $\dot{\boldsymbol{x}}_0$ (which could occur if the particle is active or elastic, or due to surface-induced flows such as a Navier slip velocity [29]). For a point $\boldsymbol{x}_1 \in S$, the two-dimensional boundary integral representation is [30]

$$\frac{1}{4\pi}\mathcal{K} - \frac{1}{4\pi\eta}\mathcal{G} = \frac{\boldsymbol{u}^{\mathrm{b}}(\boldsymbol{x}_1)}{2} + \boldsymbol{u}^{\mathrm{rg}}(\boldsymbol{x}_1) - \boldsymbol{u}^{\infty}(\boldsymbol{x}_1), \tag{4}$$

where

$$\mathcal{G} = \int_S \boldsymbol{G}(\boldsymbol{x}, \boldsymbol{x}_1) \cdot \boldsymbol{f}(\boldsymbol{x})\, \mathrm{d}\mathcal{S}(\boldsymbol{x}) \tag{5}$$

and

$$\mathcal{K} = \int_S \boldsymbol{n}(\boldsymbol{x}) \cdot \boldsymbol{K}(\boldsymbol{x}, \boldsymbol{x}_1) \cdot \boldsymbol{u}^{\mathrm{b}}(\boldsymbol{x}) \mathrm{d}\mathcal{S}(\boldsymbol{x}). \tag{6}$$

Here, the line integrals are taken over the closed boundary S, $\mathrm{d}\mathcal{S}(\boldsymbol{x})$ is a surface element, and $\boldsymbol{G}$ and $\boldsymbol{K}$ are tensors associated with the two-dimensional Green's functions for the velocity field and stress tensor, respectively. In free space, for example, the tensors are [30]

$$G_{ij}(\boldsymbol{x}, \boldsymbol{x}_1) = -\delta_{ij} \ln r + \frac{r_i r_j}{r^2}, \quad K_{ijk}(\boldsymbol{x}, \boldsymbol{x}_1) = -4\frac{r_i r_j r_k}{r^4}, \quad \boldsymbol{r} = \boldsymbol{x} - \boldsymbol{x}_1, \quad r = ||\boldsymbol{r}||. \tag{7}$$

In the formulation of (4), we have used the identity that, for a closed surface S,

$$\int_S \boldsymbol{n}(\boldsymbol{x}) \cdot \boldsymbol{K}(\boldsymbol{x}, \boldsymbol{x}_1) \cdot \boldsymbol{u}^{\mathrm{rg}}(\boldsymbol{x}) \mathrm{d}\mathcal{S}(\boldsymbol{x}) = -2\pi \boldsymbol{u}^{\mathrm{rg}}(\boldsymbol{x}_1) \tag{8}$$

for a point $\boldsymbol{x}_1 \in S$ [30]. In Eq. (4), the particle is required to be torque-and-force-free to close the system for the rigid body motion $\boldsymbol{u}^{\mathrm{rg}}$. In the limit of slender particles, $k \to 0$, Eq. (4) can be approximated by a line integral over $\boldsymbol{x}_0$, rather than over the boundary S. This line integral is regarded to be the 2D SBT.

B. 2D SBT formulation

The approach used to derive the 2D SBT representation of the boundary integral equation is to algebraically expand the kernels in Eq. (4) in a matched asymptotic expansion. This approach is similar to the method presented for slender rods as given in Ref. [31]. Specifically, the kernels in (4) are expanded to leading order in the slenderness k, for an outer scale when $s - s_1 \gg k$ and for an inner scale when $s - s_1 \ll k$. The inner and outer expansions are then used to form a composite solution corresponding to the 2D SBT in Sec. III. In the following, we will perform the expansion using a dimensionless lengthscale, normalizing length by a (thus setting $a = 1$ and $b = k$).

Before we perform the expansions of the kernels, it is useful to recast the boundary integral representation as an integral equation parametrized by $\boldsymbol{x}_0$, as our objective is to reduce the formulation to an integral equation over $\boldsymbol{x}_0$. To do so, we consider the partial derivative of the boundary S with respect to s,

$$\frac{\partial}{\partial s} S = \boldsymbol{t} \pm kh(s)\kappa \boldsymbol{t} \pm h' \hat{\boldsymbol{e}}_Y = \boldsymbol{t} + O(k\kappa, kh'). \tag{9}$$

The vector $\boldsymbol{t} = \boldsymbol{x}_0'/||\boldsymbol{x}_0'||$ is the tangent vector to the boundary and $[*]' = \partial/\partial s$. Therefore, provided the radius of curvature is much greater than the geometric aspect ratio, $1/\kappa \gg k$, and h is approximately uniform, $h'(s) \ll 1$, then the differential $\partial S/\partial s$ reduces to the tangent vector running through the particle's centerline $\boldsymbol{x}_0(s)$ and is the same for a point on the surface with a positive or negative normal from $\boldsymbol{x}_0(s)$. Under this approximation, the boundary S can be expressed as an upper curve $S^+ = \{\boldsymbol{x}_0(s) + kh(s)\hat{\boldsymbol{e}}_Y(s) : -1 \leqslant s \leqslant 1\}$ and a lower curve $S^- = \{\boldsymbol{x}_0(s) - kh(s)\hat{\boldsymbol{e}}_Y(s) : -1 \leqslant s \leqslant 1\}$, which are symmetric with respect to the centerline $\boldsymbol{x}_0$. Therefore, the integral in (5) can be recast as an integral over the top boundary as

$$\mathcal{G} = \int_S^+ [\boldsymbol{G}(\boldsymbol{x}^+, \boldsymbol{x}_1) \cdot \boldsymbol{f}(\boldsymbol{x}^+) + \boldsymbol{G}(\boldsymbol{x}^-, \boldsymbol{x}_1) \cdot \boldsymbol{f}(\boldsymbol{x}^-)] \, \mathrm{d}\mathcal{S}, \tag{10}$$

where $\boldsymbol{x}^+(s) = \boldsymbol{x}_0(s) + kh(s)\hat{\boldsymbol{e}}_Y(s)$ corresponds to a point on S^+, $\boldsymbol{x}^-(s) = \boldsymbol{x}_0(s) - kh(s)\hat{\boldsymbol{e}}_Y(s)$ corresponds to a point on S^-, and dS corresponds to a surface element on S^+. Similarly, the integral in (6) is

$$\mathcal{K} = \int_{S^+} [\boldsymbol{n}(\boldsymbol{x}^+) \cdot \boldsymbol{K}(\boldsymbol{x}^+, \boldsymbol{x}_1) \cdot \boldsymbol{u}^{\mathrm{b}}(\boldsymbol{x}^+) + \boldsymbol{n}(\boldsymbol{x}^-) \cdot \boldsymbol{K}(\boldsymbol{x}^-, \boldsymbol{x}_1) \cdot \boldsymbol{u}^{\mathrm{b}}(\boldsymbol{x}^-)] \, \mathrm{d}\mathcal{S}. \tag{11}$$

Taking advantage of the symmetry in the top and bottom surface, $\boldsymbol{f}$, $\boldsymbol{u}^\infty$, $\boldsymbol{u}^{\mathrm{b}}$, and $\boldsymbol{u}^{\mathrm{rg}}$ can all be decomposed into symmetric and antisymmetric parts with respect to $\boldsymbol{x}_0$. Given a generic vector quantity α_i, the antisymmetric part of α_i is

$$\mathrm{Asym}\{\alpha_i(\boldsymbol{x})\} = \Delta\alpha_i(\boldsymbol{x}) = \frac{\alpha_i(\boldsymbol{x}^+) - \alpha_i(\boldsymbol{x}^-)}{2} \tag{12}$$

and the symmetric part of α_i is

$$\mathrm{Sym}\{\alpha_i(\boldsymbol{x})\} = \overline{\alpha}_i(\boldsymbol{x}) = \frac{\alpha_i(\boldsymbol{x}^+) + \alpha_i(\boldsymbol{x}^-)}{2}. \tag{13}$$

With this decomposition, the integrals in Eqs. (10) and (11) are approximately

$$\mathcal{G} = \int_S^+ [(\boldsymbol{G}(\boldsymbol{x}^+, \boldsymbol{x}_1) + \boldsymbol{G}(\boldsymbol{x}^-, \boldsymbol{x}_1)) \cdot \bar{\boldsymbol{f}}(\boldsymbol{x}) + (\boldsymbol{G}(\boldsymbol{x}^+, \boldsymbol{x}_1) - \boldsymbol{G}(\boldsymbol{x}^-, \boldsymbol{x}_1)) \cdot \Delta\boldsymbol{f}(\boldsymbol{x})] \, \mathrm{d}\mathcal{S}(\boldsymbol{x}), \tag{14}$$

and

$$\begin{aligned} \mathcal{K} = \int_S^+ &[\boldsymbol{n}(\boldsymbol{x}^+) \cdot (\boldsymbol{K}(\boldsymbol{x}^+, \boldsymbol{x}_1) - \boldsymbol{K}(\boldsymbol{x}^-, \boldsymbol{x}_1)) \cdot \bar{\boldsymbol{u}}^{\mathrm{b}}(\boldsymbol{x}) \\ &+ \boldsymbol{n}(\boldsymbol{x}^+) \cdot (\boldsymbol{K}(\boldsymbol{x}^+, \boldsymbol{x}_1) + \boldsymbol{K}(\boldsymbol{x}^-, \boldsymbol{x}_1)) \cdot \Delta\boldsymbol{u}^{\mathrm{b}}(\boldsymbol{x})]\mathrm{d}\mathcal{S}(\boldsymbol{x}). \end{aligned} \tag{15}$$

For the evaluation of $\mathcal{K}$ we have used that the normal vectors on the upper and lower surface differ in sign, i.e., $\boldsymbol{n}(\boldsymbol{x}^-) = -\boldsymbol{n}(\boldsymbol{x}^+)$.

To approximate the boundary integral representation as a line integral over $\boldsymbol{x}_0$ also requires the decomposition of the flow field on $\boldsymbol{x}_0$. To do so, we compute the average flow field, corresponding to the average flow between a point on the upper surface $\boldsymbol{x}_1^+(s_1) \in S^+$ and a point on the lower surface $\boldsymbol{x}_1^-(s_1) \in S^-$. The average flow field on the point $\boldsymbol{x}_0(s_1)$ is thus

$$\bar{\boldsymbol{u}}(s_1) = \frac{1}{2}\left\{\left(\frac{\boldsymbol{u}^{\mathrm{b}}(\boldsymbol{x}_1^+)}{2} + \boldsymbol{u}^{\mathrm{rg}}(\boldsymbol{x}_1^+) - \boldsymbol{u}^\infty(\boldsymbol{x}_1^+)\right) + \left(\frac{\boldsymbol{u}^{\mathrm{b}}(\boldsymbol{x}_1^-)}{2} + \boldsymbol{u}^{\mathrm{rg}}(\boldsymbol{x}_1^-) - \boldsymbol{u}^\infty(\boldsymbol{x}_1^-)\right)\right\}. \tag{16}$$

In addition to computing the average, we also compute the flow difference between the top and bottom surface at the point $\boldsymbol{x}_0(s_1)$. The flow difference is

$$\Delta\boldsymbol{u}(s_1) = \frac{1}{2}\left\{\left(\frac{\boldsymbol{u}^{\mathrm{b}}(\boldsymbol{x}_1^+)}{2} + \boldsymbol{u}^{\mathrm{rg}}(\boldsymbol{x}_1^+) - \boldsymbol{u}^\infty(\boldsymbol{x}_1^+)\right) - \left(\frac{\boldsymbol{u}^{\mathrm{b}}(\boldsymbol{x}_1^-)}{2} + \boldsymbol{u}^{\mathrm{rg}}(\boldsymbol{x}_1^-) - \boldsymbol{u}^\infty(\boldsymbol{x}_1^-)\right)\right\}. \tag{17}$$

The flow difference $\Delta\boldsymbol{u}(s_1)$ scales with the thickness k of the particle. Since for vanishing thickness this flow field is subdominant to $\bar{\boldsymbol{u}}(s_1)$, it may be assumed that it could be neglected. However, we will demonstrate in Sec. V that, for some special cases, the flow difference must be retained. In particular, considering a straight (unbent) particle, it can be shown that the symmetric part of the traction $\bar{\boldsymbol{f}}$ can also scale with the thickness of the particle, and thus the $O(k)$ terms can become important for obtaining the leading-order values of $\bar{\boldsymbol{f}}$.

The boundary integral equations for $\bar{\boldsymbol{u}}$ and $\Delta \boldsymbol{u}$ are

$$\frac{1}{4\pi}\bar{\mathcal{K}} - \frac{1}{4\pi\eta}\bar{\mathcal{G}} = \bar{\boldsymbol{u}}(s_1) \tag{18}$$

and

$$\frac{1}{4\pi}\Delta\mathcal{K} - \frac{1}{4\pi\eta}\Delta\mathcal{G} = \Delta\boldsymbol{u}(s_1), \tag{19}$$

where $\bar{\mathcal{G}} = (1/2)[\mathcal{G}(\boldsymbol{x}_1^+) + \mathcal{G}(\boldsymbol{x}_1^-)]$, $\bar{\mathcal{K}} = (1/2)[\mathcal{K}(\boldsymbol{x}_1^+) + \mathcal{K}(\boldsymbol{x}_1^-)]$, $\Delta\mathcal{G} = (1/2)[\mathcal{G}(\boldsymbol{x}_1^+) - \mathcal{G}(\boldsymbol{x}_1^-)]$, and $\Delta\mathcal{K} = (1/2)[\mathcal{K}(\boldsymbol{x}_1^+) - \mathcal{K}(\boldsymbol{x}_1^-)]$. We will see that the decomposition given in (18) and (19) is particularly useful to obtain a matched asymptotic expansion of the boundary integral representation for $k \to 0$, in terms of the average flow/flow difference over $\boldsymbol{x}_0$.

C. Outer region

The outer expansion of Eqs. (18) and (19) is obtained by expanding the kernels in (18) and (19) for $k \to 0$, assuming $s - s_1 \gg k$. For a generic function $\mathcal{F}(\boldsymbol{x}_0(s) \pm kh(s)\hat{\boldsymbol{e}}_Y)$, the expansion for small k is

$$\begin{aligned}\mathcal{F}(\boldsymbol{x}_0(s)) \pm kh(s)\hat{\boldsymbol{e}}_Y &= \mathcal{F}(s) \pm kh(s)[\sin\theta, \cos\theta] \cdot \left[\left.\frac{\partial \mathcal{F}}{\partial X_0}\right|_{k=0}, \left.\frac{\partial \mathcal{F}}{\partial Y_0}\right|_{k=0} \right] + O(k^2) \\ &= \mathcal{F}(s) \pm kh(s)\left(\sin\theta \left.\frac{\partial \mathcal{F}}{\partial X_0}\right|_{k=0} + \cos\theta \left.\frac{\partial \mathcal{F}}{\partial Y_0}\right|_{k=0} \right) + O(k^2).\end{aligned} \tag{20}$$

For this expansion, we used that $\hat{\boldsymbol{e}}_Y = \cos\theta\hat{\boldsymbol{e}}_{Y_0} + \sin\theta\hat{\boldsymbol{e}}_{X_0}$, as given in (1). We have also introduced the shorthand notation $\mathcal{F}(s) \equiv \mathcal{F}(\boldsymbol{x}_0(s))$, which we use from hereon for all functions that depend only on $\boldsymbol{x}_0(s)$. We use Eq. (20) to expand $\boldsymbol{G}$ and $\boldsymbol{K}$ in Eqs. (18) and (19). The outer expansion of the term $\bar{\mathcal{G}}$ is

$$\bar{\mathcal{G}}^{\text{out}} = \int_{\mathcal{L}} \left[2\bar{\boldsymbol{f}} \cdot \boldsymbol{G}(s, s_1) + 2kh(s)\Delta\boldsymbol{f} \cdot \left(\sin\theta \left.\frac{\partial \boldsymbol{G}}{\partial X_0}\right|_{k=0} + \cos\theta \left.\frac{\partial \boldsymbol{G}}{\partial Y_0}\right|_{k=0} \right) \right] \mathrm{d}L(s) + O(k^2). \tag{21}$$

The integrals are now taken over the line $\mathcal{L}$ corresponding to the centerline $\boldsymbol{x}_0$ with line element $\mathrm{d}L(s)$, and, in the expansion, we used $h(s) \approx h(s_1)$ over the slender portion of the surface. The outer expansion of $\Delta\mathcal{G}$ is

$$\Delta\mathcal{G}^{\text{out}} = -2k \int_{\mathcal{L}} h(s)\bar{\boldsymbol{f}} \cdot \left(\sin\theta \left.\frac{\partial \boldsymbol{G}}{\partial X_0}\right|_{k=0} + \cos\theta \left.\frac{\partial \boldsymbol{G}}{\partial Y_0}\right|_{k=0} \right) \mathrm{d}L(s) + O(k^2). \tag{22}$$

This term scales with k to leading order. The outer expansion of $\bar{\mathcal{K}}$ is

$$\begin{aligned}\bar{\mathcal{K}}^{\text{out}} = \int_{\mathcal{L}} \Bigg[& 2\boldsymbol{n}(s) \cdot \boldsymbol{K}(s, s_1) \cdot \Delta\boldsymbol{u}^{\text{b}}(s) \\ & + 2kh(s)\boldsymbol{n}(s) \cdot \left(\sin\theta \left.\frac{\partial \boldsymbol{K}}{\partial X_0}\right|_{k=0} + \cos\theta \left.\frac{\partial \boldsymbol{K}}{\partial Y_0}\right|_{k=0} \right) \cdot \bar{\boldsymbol{u}}^{\text{b}}(s) \Bigg] \mathrm{d}L(s) + O(k^2).\end{aligned} \tag{23}$$

Since $\Delta\boldsymbol{u}^{\text{b}}(s)$ scales with k, Eq. (23) also scales with k to leading order. Lastly, it can be shown by direct dimensional analysis that the expansion of the term $\Delta\mathcal{K}^{\text{out}}$ scales as $O(k^2)$, and is therefore subdominant.

D. Inner region

The evaluation of the inner expansions of Eqs. (18) and (19) requires expanding (18) and (19) when $s - s_1 \ll k$. To do so, we first rescale the variable s into an inner variable χ by setting

$\epsilon\chi = s - s_1$ for some arbitrary small constant $\epsilon \ll 1$. As $\chi \to 0$, $\boldsymbol{G}$ and $\boldsymbol{K}$ are singular. We will use the singular behavior of $\boldsymbol{G}$ and $\boldsymbol{K}$ to evaluate the leading contribution to the integrals in (18) and (19) about this singular point, $\chi = 0$, up to $O(k)$. Independent of the choice of $\boldsymbol{G}$ and $\boldsymbol{K}$, the singular behavior of $\boldsymbol{G}$ and $\boldsymbol{K}$ can always be described exactly by that of the free-space tensors [30], which are given in Eq. (7). We thus use the free-space tensors to evaluate the integrals in (18) and (19) in this inner region, about the singular point. We note that the regular portion of $\boldsymbol{G}$ and $\boldsymbol{K}$ will not contribute to a $O(k)$ dependence, and thus we do not consider the effect of the regular parts in the expansion.

Taking advantage of the singular structure in $\boldsymbol{G}$ and $\boldsymbol{K}$, we then Taylor-expand $\boldsymbol{f}(s)$, $h(s)$, and $\boldsymbol{u}^{\mathrm{b}}(s)$ about the singular point $s = s_1$, which corresponds to the point $\chi = 0$ in inner variables. To leading order in this expansion, we have $h(s) = h(s_1)$, which corresponds to the particle having a rectangular cross-section with uniform thickness $h(s_1)\hat{\boldsymbol{e}}_Y$. To evaluate the integrals for $\chi \to 0$, we thus first project (18) and (19) onto the $\hat{\boldsymbol{e}}_X$ and $\hat{\boldsymbol{e}}_Y$ space as

$$\hat{\boldsymbol{e}}_X \cdot \left(\frac{1}{4\pi}\bar{\mathcal{K}}[\boldsymbol{n}, \boldsymbol{u}^{\mathrm{b}}] - \frac{1}{4\pi\eta}\bar{\boldsymbol{\mathcal{G}}}\right) = \bar{u}_X(\boldsymbol{x}_1), \quad \hat{\boldsymbol{e}}_Y \cdot \left(\frac{1}{4\pi}\bar{\mathcal{K}}[\boldsymbol{n}, \boldsymbol{u}^{\mathrm{b}}] - \frac{1}{4\pi\eta}\bar{\boldsymbol{\mathcal{G}}}\right) = \bar{u}_Y(\boldsymbol{x}_1) \tag{24}$$

and

$$\hat{\boldsymbol{e}}_X \cdot \left(\frac{1}{4\pi}\Delta\mathcal{K}[\boldsymbol{n}, \boldsymbol{u}^{\mathrm{b}}] - \frac{1}{4\pi\eta}\Delta\boldsymbol{\mathcal{G}}\right) = \Delta u_X(\boldsymbol{x}_1), \quad \hat{\boldsymbol{e}}_Y \cdot \left(\frac{1}{4\pi}\Delta\mathcal{K}[\boldsymbol{n}, \boldsymbol{u}^{\mathrm{b}}] - \frac{1}{4\pi\eta}\Delta\boldsymbol{\mathcal{G}}\right) = \Delta u_Y(\boldsymbol{x}_1). \tag{25}$$

This projection corresponds to a frame of reference aligned with the axes of symmetry of the rectangular cross-section. The integrals are then evaluated analytically at leading order in the expansion for the case $\epsilon \to 0$ and up to $O(k)$. The leading contribution to the inner expansions of the terms for $\bar{\boldsymbol{\mathcal{G}}}$ and $\Delta\boldsymbol{\mathcal{G}}$ for $\epsilon \to 0$ comes from

$$\begin{aligned}\Delta\mathcal{G}_X(\boldsymbol{x}_1) \equiv \hat{\boldsymbol{e}}_X \cdot \Delta\boldsymbol{\mathcal{G}}(\boldsymbol{x}_1) \approx \lim_{\epsilon\to 0}\frac{1}{2}\Bigg\{&\Delta f_X(s_1)\int_{-1/\epsilon}^{1/\epsilon}[G^*_{XX}(\epsilon\chi, 0) - G^*_{XX}(\epsilon\chi, -2h(s_1))]\mathrm{d}\chi \\ &- \Delta f_X(s_1)\int_{-1/\epsilon}^{1/\epsilon}[G^*_{XX}(\epsilon\chi, 2h(s_1)) - G^*_{XX}(\epsilon\chi, 0)]\mathrm{d}\chi\Bigg\} \\ =\ & 4\pi k h(s_1)\Delta f_X(s_1) + O(k^2).\end{aligned} \tag{26}$$

All other components of the inner expansion of $\bar{\boldsymbol{\mathcal{G}}}$ and $\Delta\boldsymbol{\mathcal{G}}$ are zero at $O(k)$. To compute the expansion given in Eq. (26), we have introduced a new term $G^*_{XX}(X, Y)$. This term corresponds to the component of G_{XX} given in (7), but with a slightly different notation used to compute its value,

$$G^*_{XX}(X, Y) = -\ln(\sqrt{X^2 + Y^2}) + \frac{X^2}{X^2 + Y^2}. \tag{27}$$

Under this notation, it follows that for a rectangle cross-section of uniform thickness $h(s) = h(s_1)$, the integrands in $\Delta\mathcal{G}_X(\boldsymbol{x}_1)$ simplify to $G_{XX}(\boldsymbol{x}^+, \boldsymbol{x}_1) = G^*_{XX}(s - s_1, h(s) - h(s_1)) = G^*_{XX}(\epsilon\chi, 0)$ and $G_{XX}(\boldsymbol{x}^-, \boldsymbol{x}_1) = G^*_{XX}(s - s_1, -h(s) - h(s_1)) = G^*_{XX}(\epsilon\chi, -2h(s_1))$. Evaluating the integral in (26) in the limit $\epsilon \to 0$ and then Taylor-expanding the remaining integral for small k gives the result on the right-hand side of (26). We use the same approach to evaluate the leading contribution to the inner expansion of the term $\bar{\mathcal{K}}$. The result is

$$\begin{aligned}\bar{\mathcal{K}}_X(\boldsymbol{x}_1) &\equiv \hat{\boldsymbol{e}}_X \cdot \bar{\mathcal{K}}(\boldsymbol{x}_1)\\ &\approx \lim_{\epsilon\to 0}\frac{1}{2}\left\{\bar{u}_X^{\mathrm{b}}(s_1)n_Y(s_1)\int_{-1/\epsilon}^{1/\epsilon}[K_{XXY}^*(\epsilon\chi, 2h(s_1)) - K_{XXY}^*(\epsilon\chi, -2h(s_1))]\mathrm{d}\chi\right\}\\ &= -2\pi\bar{u}_X^{\mathrm{b}}(s_1) + O(k^2)\end{aligned} \tag{28}$$

and

$$\begin{aligned}\bar{\mathcal{K}}_Y(\boldsymbol{x}_1) &\equiv \hat{\boldsymbol{e}}_Y \cdot \bar{\mathcal{K}}(\boldsymbol{x}_1)\\ &\approx \lim_{\epsilon\to 0}\frac{1}{2}\left\{\bar{u}_Y^{\mathrm{b}}(s_1)n_Y(s_1)\int_{-1/\epsilon}^{1/\epsilon}[K_{YYY}^*(\epsilon\chi, 2h(s_1)) - K_{YYY}^*(\epsilon\chi, -2h(s_1))]\mathrm{d}\chi\right\}\\ &= -2\pi\bar{u}_Y^{\mathrm{b}}(s_1) + O(k^2).\end{aligned} \tag{29}$$

We have used that $n_Y = 1$ and $n_X = O(k^2)$ for this computation. The terms

$$K_{XXY}^*(X,Y) = -4\frac{XXY}{(X^2+Y^2)^2}, \quad K_{YYY}^*(X,Y) = -4\frac{YYY}{(X^2+Y^2)^2} \tag{30}$$

are the same as the specific components for the tensor K_{ijk} given in (7), but with a slightly different notation used to compute its value. All other terms are equal to $O(k^2)$, or greater, and are thus subdominant. Likewise, the dominant terms for the inner expansion of $\Delta\mathcal{K}$ are

$$\begin{aligned}\Delta\mathcal{K}_X(\boldsymbol{x}_1) &\equiv \hat{\boldsymbol{e}}_X \cdot \Delta\mathcal{K}(\boldsymbol{x}_1)\\ &\approx \lim_{\epsilon\to 0}\frac{1}{2}\left\{\bar{u}_X^{\mathrm{b}}(s_1)n_Y(s_1)\int_{-1/\epsilon}^{1/\epsilon}[K_{XXY}^*(\epsilon\chi, -2h(s_1)) - K_{XXY}^*(\epsilon\chi, 2h(s_1))]\mathrm{d}\chi\right\}\\ &= 2\pi\Delta u_X^{\mathrm{b}}(s_1) + O(k^2)\end{aligned} \tag{31}$$

and

$$\begin{aligned}\Delta\mathcal{K}_Y(\boldsymbol{x}_1) &\equiv \hat{\boldsymbol{e}}_X \cdot \Delta\mathcal{K}(\boldsymbol{x}_1)\\ &\approx \lim_{\epsilon\to 0}\frac{1}{2}\left\{\bar{u}_Y^{\mathrm{b}}(s_1)n_Y(s_1)\int_{-1/\epsilon}^{1/\epsilon}[K_{YYY}^*(\epsilon\chi, -2h(s_1)) - K_{YYY}^*(\epsilon\chi, 2h(s_1))]\mathrm{d}\chi\right\}\\ &= 2\pi\Delta u_Y^{\mathrm{b}}(s_1) + O(k^2).\end{aligned} \tag{32}$$

The leading effect of the inner expansion for $\bar{\mathcal{K}}$ in (24) corresponds to $\bar{\boldsymbol{u}}^{\mathrm{b}}$ satisfying the identity given in Eq. (8) for $\bar{\boldsymbol{u}}^{\mathrm{rg}}$ to leading order. Therefore, the inner expansion for the average velocity on $\boldsymbol{x}_0$, given by (24), is approximately

$$\bar{\boldsymbol{u}} + \bar{\boldsymbol{u}}^{\mathrm{b}}/2 \equiv \bar{\boldsymbol{u}}^{\mathrm{rg}} + \bar{\boldsymbol{u}}^{\mathrm{b}} - \bar{\boldsymbol{u}}^{\infty} = \boldsymbol{0}. \tag{33}$$

This condition corresponds to the motion of the particle following exactly the motion of the flow.

For the inner expansion of the average velocity difference on $\boldsymbol{x}_0$, given by (25), an identity similar to (8) is also obtained in Eqs. (31) and (32), but with a change in sign. In this case, the approximation $\Delta\boldsymbol{K} = 2\pi\Delta\boldsymbol{u}^b$ corresponds to the term $\Delta\boldsymbol{u}^b$ canceling exactly in (25) to leading order. The inner expansion for (25) is thus approximately

$$-\frac{1}{\eta}kh(s_1)\Delta f_X(s_1)\hat{\boldsymbol{e}}_X = \Delta\boldsymbol{u} - \Delta\boldsymbol{u}^{\mathrm{b}}/2 \equiv \Delta\boldsymbol{u}^{\mathrm{rg}} - \Delta\boldsymbol{u}^{\infty}. \tag{34}$$

Therefore, the flow difference is controlled by the tangential shear stress difference over each element on $\boldsymbol{x}_0$, balanced with the linear motion produced by the flow and the particle.

In the next section, we provide the composite solution resulting from the derivation presented here, which can be directly implemented for numerical simulations.

III. SBT THEORY FOR A TWO-DIMENSIONAL PLATE: OVERVIEW AND GUIDELINES

A. The composite solution

The composite solution, corresponding to the 2D SBT, is obtained by matching the outer and inner expansions of the kernels in the boundary integral representation, derived in Sec. II. Some terms of the expanded kernels can be common to both the outer and inner regions [32]. The advantage of evaluating $\bar{\boldsymbol{u}}$ and $\Delta\boldsymbol{u}$, which correspond to the average flow and the average flow difference over the particle's longitudinal center $\boldsymbol{x}_0$, is that the common parts of these kernels are now zero by construction. This can be verified by rewriting the outer solution (21)–(23) in inner variables $\epsilon\chi = s - s_1$ and taking the limit of $\epsilon \to 0$ [32]. The 2D SBT is thus equal to the composite solution of the outer and inner expansions. The result for the average flow field on $\boldsymbol{x}_0$ is, to $O(k)$,

$$\frac{1}{4\pi}\bar{\mathcal{K}}^{\text{out}} - \frac{1}{4\pi\eta}\bar{\mathcal{G}}^{\text{out}} = \bar{\boldsymbol{u}}^{\text{rg}} + \bar{\boldsymbol{u}}^{\text{b}} - \bar{\boldsymbol{u}}^{\infty}. \tag{35}$$

Here, we recall that the $[\bar{*}]$ corresponds to the average of [*] from the top and bottom surface about the point $\boldsymbol{x}_0(s)$, and $\Delta[*]$ is the difference. The additional requirement that $\bar{\boldsymbol{f}}$ and $\Delta\boldsymbol{f}$ must satisfy the force-and-torque-free condition is needed for the computation of $\bar{\boldsymbol{u}}^{\text{rg}}$. The result for the average flow difference on $\boldsymbol{x}_0$ is, to $O(k)$,

$$\Delta\boldsymbol{u}^{\infty} - \Delta\boldsymbol{u}^{\text{rg}} = \frac{1}{\eta}kh(s_1)\Delta f_X(s_1)\hat{\boldsymbol{e}}_X - \frac{1}{2\pi\eta}k\int_{\mathcal{L}} h(s)\bar{\boldsymbol{f}}\cdot\left(\sin\theta\,\frac{\partial\boldsymbol{G}}{\partial X_0}\bigg|_{k=0} + \cos\theta\,\frac{\partial\boldsymbol{G}}{\partial Y_0}\bigg|_{k=0}\right)\mathrm{d}L(s). \tag{36}$$

The terms $\bar{\mathcal{G}}^{\text{out}}$ and $\bar{\mathcal{K}}^{\text{out}}$ are given in Eqs. (21) and (23), respectively.

B. Simplifications of the 2D SBT equation for curved particles

If the slender body is sufficiently bent, then the terms of order k or greater become subdominant, and the 2D SBT can be approximated by

$$\bar{\boldsymbol{u}}^{\text{rg}} + \bar{\boldsymbol{u}}^{\text{b}} - \bar{\boldsymbol{u}}^{\infty} = -\frac{1}{2\pi\eta}\int_{\mathcal{L}}[\bar{\boldsymbol{f}}\cdot\boldsymbol{G}(s, s_1)]\mathrm{d}L(s). \tag{37}$$

This equation represents a line distribution of point forces over the centerline, where the forces are orientated in the direction of motion of the two-dimensional sheet. A similar equation has already been suggested to model infinitesimal thin disks [30] and to model the dynamics, for example, of two-dimensional flexible sheets [23–25]. The difference is that in these citations, a prefactor $1/4\pi\eta$ has been used instead of the $1/2\pi\eta$ prefactor in (37), which is the case if just one surface of the sheet is considered. The $1/2\pi\eta$ prefactor in (37) is due to the interaction over the top and bottom surfaces. For the cases of modeling a flexible sheet in Refs. [23–25], this effect can simply be accounted for by a change in the prefactor of the deformation of the sheet by a factor of 2.

C. Guidelines for using the 2D SBT equation

The 2D SBT model is designed to be used when the effect of the edges on the fluid-structure interaction of ultrathin particles is negligible, which is the case for plates and sheetlike particles in many flow conditions, as we will demonstrate in the validation cases in Secs. IV–VI. Modeling the fluid-structure interaction at the edge of ultrathin particles is nontrivial since it requires a resolution much smaller than the particle thickness (see, for example, Ref. [4]). Excluding the discretization of edges in the 2D SBT can thus significantly reduce computational cost. However, there are special cases when edge effects can become important. Such examples include when a straight particle is aligned with its longitudinal axis in the direction of shear flow [33], when there is sufficient hydrodynamic slip [29,34,35], or when the flow past a wall with slits is considered [36,37]. In these cases, the 2D SBT will fail to predict the correct fluid-structure interaction of the particles. There are strategies to include the effect of the edges into a slender-body-type approximation, such as that suggested by Ref. [38], or by using known analytical solutions to flows around a pointed corner [39,40]. However, as shown computationally and analytically for the rotational dynamics of axisymmetric disk particles in a linear flow field [33], the particular shape of the edge (e.g., a tapered cone shape or a blunted rectangular-shape edge) strongly affects the rotational dynamics of the particles for a small range of particle orientation close to the flow direction. Thus, to adapt our 2D SBT model to include edge effects, the specific edge shape of the particle must be considered. Otherwise, a higher-order method, which takes into account the edges of the particle, such as the boundary integral method [30], Lorentz Reciprocal theorem [41], or the Finite-Element Method [4], is required to resolve the correct fluid-structure interaction.

In Sec. V we give an outline on how to compute the accuracy of our 2D SBT model in resolving the motion of a particle freely suspended in a linear flow field. For the cases in which the 2D SBT fails in predicting the motion of the particle, 2D SBT can still be used to compute some important information about the flow and rheology of the particle. Specifically, when using the full $O(k)$ accurate 2D SBT given in (35) and (36), it is still possible to accurately resolve the average traction distribution over the slender portion of the boundary comprising the two-dimensional particle, for the computation of the stress tensor acting on a straight (undeformed) no-slip particle in a shear flow field (as shown in Sec. V), or for the computation of the torques and forces acting on the particle when held fixed with its major axes perpendicular to the flow direction (as shown in Refs. [29,33,34]).

One drawback in excluding the effect of the edges is that, for a line distribution of point forces, given in Eqs. (37) or (35) and (36), the traction $\boldsymbol{f}$ can diverge logarithmically at the edges of the line ($s = \pm 1$), due to the logarithmic singularity in $\boldsymbol{G}$. In general, the logarithmic divergence of $\boldsymbol{f}$ at the tip of the particle is still integrable, and thus 2D SBT can still be used to compute well-posed quantities of interest, such as the torque and force acting on a curved particle in a shear flow field (see Sec. IV), or the average translational velocity of a finite swimming two-dimensional sheet (see Sec. VI). In reality, the logarithmic singularity is prevented because of the edges of the particle. The effect of the thickness of the particle vanishing at the tip or edge of the particle is to create a dipole in $\boldsymbol{f}$ that occurs near the tip of the particle itself [33]. This dipole prevents $\boldsymbol{f}$ from diverging, although its value can still be large [33]. The dipole occurs in a boundary region from the edge, whose size scales as a power law with k and depends on the particular shape of the particle [33].

In the formulation of the 2D SBT model, the boundary condition on the particle's surface has not been specified. Our formulation is not restrictive to the type of boundary condition such as no-slip or Navier slip [42]. However, the boundary condition must be such that dominant hydrodynamic traction still occurs over the particle's surface and not at the edges for the 2D SBT to be valid.

Our formulation is also not restrictive to the type of Green's function used, as long as the Green's function is defined for two-dimensional flow. For example, the Green's functions for two-dimensional flow in free space, a point above a wall, an array of point forces, or a point force between two plates [30] could all be used in our 2D SBT formulation. An example of the 2D SBT for a one-dimensional periodic Green's function is presented in Sec. VI.

IV. VALIDITY OF 2D SBT: CIRCULAR ARC IN SHEAR

We compare computations from our 2D SBT to analytical computations for the motion of a two-dimensional circular arc of infinitesimal thickness, immersed in an external shear flow field $\boldsymbol{u}^{\infty} = \dot{\gamma} y \hat{\boldsymbol{e}}_x$ [26]. The arc is assumed to lie in the two-dimensional plane parametrized by the Cartesian coordinate system $x\hat{\boldsymbol{e}}_x + y\hat{\boldsymbol{e}}_y$, as sketched in Fig. 2. Assuming the arc to be rigid, the arc follows a rigid-body motion $\boldsymbol{u}^{\mathrm{rg}} = \boldsymbol{U} + \Omega\hat{\boldsymbol{e}}_z \times \boldsymbol{x}_m$ for some translation velocity $\boldsymbol{U}$ and angular velocity Ω. The arc is parametrized in terms of the orientation angle θ between the arc's tangent and the positive horizontal axis $\hat{\boldsymbol{e}}_x$. Under this notation, the analytical value of the rigid-body motion for an arc of

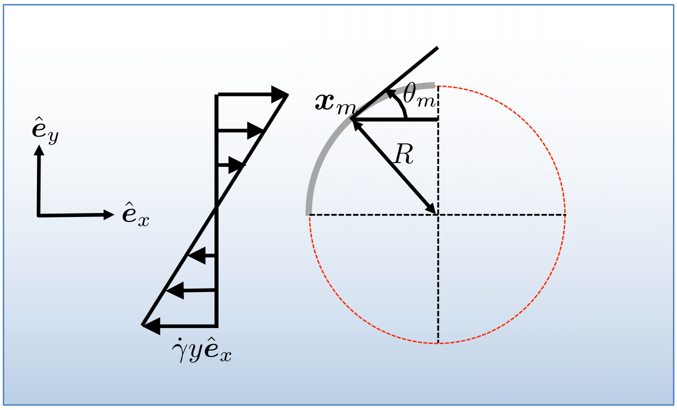

FIG. 2. Sketch of a slender two-dimensional arc in an external shear flow field.

radius R and arclength $R\Delta\theta$ is [26]

$$U_x = \dot{\gamma} y_m - \frac{\dot{\gamma} R}{2}\left[1 - \cos^4\left(\frac{\Delta\theta}{4}\right)\right]\cos\theta_m, \tag{38}$$

$$U_y = -\frac{\dot{\gamma} R}{2}\left[1 - \cos^4\left(\frac{\Delta\theta}{4}\right)\right]\sin\theta_m, \tag{39}$$

$$\Omega = -\frac{\dot{\gamma}}{2}\left[1 - \cos^2\left(\frac{\Delta\theta}{4}\right)\cos 2\theta_m\right]. \tag{40}$$

Here $\Delta\theta \in (0, 2\pi]$ is the positive difference between the value of θ at each end of the arc. The motion depends on the midpoint of the arc $\boldsymbol{x}_m = (x_m, y_m)$ and the orientation angle θ_m between the arc's tangent at $\boldsymbol{x}_m$ and the positive horizontal axis, as sketched in Fig. 2.

A complex variable method was used to analytically solve the incompressible Stokes equation for the arc to obtain Eqs. (38)–(40). Here, we show that this same result can be obtained by evaluating the 2D SBT equation, given in (37), either numerically (as for the case for $\Delta\theta \neq 2\pi$) or analytically for $\Delta\theta = 2\pi$, which corresponds to a circle. Parametrizing the arc's central line $\boldsymbol{x}_0$ in terms of the angle θ by $\boldsymbol{x}_0 = (R(\cos\theta - \cos\theta_m), R(\sin\theta - \sin\theta_m))$ for $\theta \in (\theta_m - \Delta\theta/2, \theta_m + \Delta\theta/2)$, the 2D SBT equation, (37), becomes

$$\frac{1}{2\pi\eta}\int_{\theta_m+\Delta\theta/2}^{\theta_m-\Delta\theta/2} (\bar{f}_x G_{xx}(\theta,\theta_1) + \bar{f}_y G_{yx}(\theta,\theta_1)) R\mathrm{d}\theta = (\dot{\gamma} + \Omega) y(\theta_1) - U_x, \tag{41}$$

$$\frac{1}{2\pi\eta}\int_{\theta_m+\Delta\theta/2}^{\theta_m-\Delta\theta/2} (\bar{f}_y G_{yy}(\theta,\theta_1) + \bar{f}_x G_{xy}(\theta,\theta_1)) R\mathrm{d}\theta = -\Omega x(\theta_1) - U_y. \tag{42}$$

The tensor $\boldsymbol{G}$ corresponds to the tensor associated with the free-space Green's function given in (7).

A. Comparison for a circle ($\Delta\theta = 2\pi$)

For $\Delta\theta = 2\pi$, the centerline of the arc forms a circle for which Eqs. (41) and (42) can be solved analytically. Without loss of generality, we set $\theta_m = 0$. Since $\boldsymbol{x}_0$ is now periodic, the traction $\bar{\boldsymbol{f}}$ can be expressed as a Fourier series for θ,

$$\bar{f}_x(\theta) = a_{x,0} + \sum_{n=1}^{n=\infty} a_{x,n}\cos(n\theta) + b_{x,n}\sin(n\theta), \tag{43}$$

$$\bar{f}_y(\theta) = a_{y,0} + \sum_{n=1}^{n=\infty} a_{y,n}\cos(n\theta) + b_{y,n}\sin(n\theta). \tag{44}$$

Substituting (43) and (44) into (41) and (42), the integrands in (41) and (42) can be computed exactly. Equating each equation at each Fourier mode forms a set of linear equations for the Fourier coefficients. Solving the set of linear equations gives

$$\bar{f}_x = \frac{3\dot{\gamma} + 2\Omega}{2}\sin(\theta) + b_{x,1}\cos(\theta), \quad \bar{f}_y = \frac{\dot{\gamma} - 2\Omega}{2}\cos(\theta) + b_{x,1}\sin(\theta), \tag{45}$$

and

$$U_x = \dot{\gamma} y_m + \Omega y_m, \quad U_y = -\Omega x_m. \tag{46}$$

In this computation, we have also used the condition of zero net total force. All other Fourier coefficients are vanishing.

The terms proportional to $b_{x,1}$ in (45) are the result of $\bar{\boldsymbol{f}}$ being uniquely defined up to the coefficient $p_0\boldsymbol{n}$ for some arbitrary pressure $p_0 = b_{x,1}$ and the surface normal vector $\boldsymbol{n}$ [43]. The term "$p_0\boldsymbol{n}$" does not affect the values of the rigid-body motion and is an arbitrary prefactor obtained from solving the incompressible Stokes equations [43]. Without loss of generality, we set $b_{x,1} = 0$.

Equation (45) can be used to compute the total torque acting on the arc by

$$T = 2\int_0^{2\pi} R(\bar{f}_x y - \bar{f}_y x)\mathrm{d}\theta = 2\pi R(2\Omega + \dot{\gamma}). \tag{47}$$

For a torque-free body, the constraint $T = 0$ is hence satisfied for

$$\Omega = -\frac{\dot{\gamma}}{2}, \quad U_x = \dot{\gamma} y_m - \frac{R\dot{\gamma}}{2}\cos\theta_m, \quad U_y = \frac{R\dot{\gamma}}{2}\sin\theta_m, \tag{48}$$

in agreement with the analytical values given in Eqs. (38)–(40) for $\Delta\theta = 2\pi$.

B. Numerical evaluation of the 2D SBT for circular arcs $0 < \Delta\theta < 2\pi$

When $\Delta\theta \neq 2\pi$, Eqs. (41) and (42) need to be computed numerically to find the rigid-body motion. To do so, $\boldsymbol{x}_0$ is discretized into N evenly spaced arc elements. The traction $\bar{\boldsymbol{f}}$ is discretized as a piecewise continuous function over the midpoint of each arc element. The leading 2D SBT equation, given in (41) and (42), is then evaluated numerically over each element using a 20-point Gauss-Legendre quadrature. If the element is singular, the logarithmic singularity in the tensor $\boldsymbol{G}$ is subtracted off and evaluated analytically [43]. The remainder of the integral is regular and so is integrated as for a regular element. The discretized equations, along with the discretized equations for zero net force and torque, form a linear system for the discrete traction vectors and Ω, U_x, and U_y. These equations are then solved by Gaussian elimination to find the discrete traction vectors and Ω, U_x, and U_y.

Figure 3 shows the normalized maximum error between the computed values of Ω, obtained from solving the 2D SBT numerically, with the analytical value (40) as a function of space and for $\Delta\theta = \pi$ and 0.01π. The maximum error decreases inversely with N as N increases, as expected from the spatial discretization of $\bar{\boldsymbol{f}}$ [44].

Figure 4 compares the analytical values of Ω, U_x, and U_y, given in Eqs. (38)–(40), with computed values of the 2D SBT. The comparison confirms good agreement with the 2D SBT computations to the analytical values for all $\Delta\theta$ and selected values of θ_m.

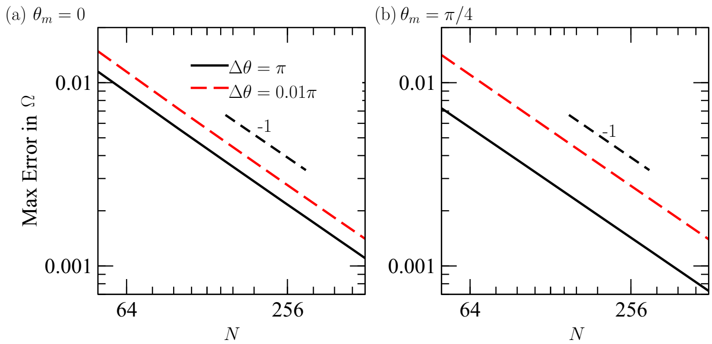

FIG. 3. Comparison of the maximum normalized error between values of Ω obtained from solving the 2D SBT with values from Eq. (40) vs N. In computations, (a) $\theta_m = 0$ or (b) $\theta_m = \pi/4$, and $\Delta\theta = \pi$ (black solid line) or $\Delta\theta = 0.01\pi$ (red-dashed line), $\boldsymbol{x}_m = 0$, and $R = 2/\Delta\theta$.

V. VALIDITY OF 2D SBT: STRAIGHT PLATELIKE PARTICLE IN SHEAR

The limit $\Delta\theta \to 0$ corresponds to a straight arc of vanishing thickness, whose motion we will show can still be predicted by 2D SBT. For this case, we parametrize $\boldsymbol{x}_0$ in terms of the particle's tangential length X as $\{\boldsymbol{x}_0 = X\hat{\boldsymbol{e}}_X : X = [-1, 1]\}$, where $\hat{\boldsymbol{e}}_X$ is the unit vector in the direction of the particle's tangent. The half-thickness of the particle is given by $kh(X)\hat{\boldsymbol{e}}_Y$. Under this notation, we will show that the 2D SBT can be used to obtain predictions on (i) $\boldsymbol{u}^{\mathrm{rg}}$ and (ii) the stresslet tensor for two-dimensional flow [30], up to $O(k)$. The stresslet tensor is defined as [30]

$$S_{ij}(\theta_m) = \frac{1}{2}\int_S \left[f_i(\theta_m)x_j + f_j(\theta_m)x_i - 2\eta\left(u_i^{\mathrm{b}}n_j + u_j^{\mathrm{b}}n_i\right)\right]\mathrm{d}\mathcal{S}, \tag{49}$$

where x_i is the position vector with respect to the particle's geometric center [30].

Given θ_m, the stresslet tensor can be used to compute the instantaneous intrinsic viscosity coefficient α or the instantaneous normal stress difference β [45,46]. For two-dimensional flow [29,47],

$$\alpha(\theta_m) = A(1 - \cos 4\theta_m) + B \tag{50}$$

and

$$\beta(\theta_m) = 2A(\sin 4\theta_m). \tag{51}$$

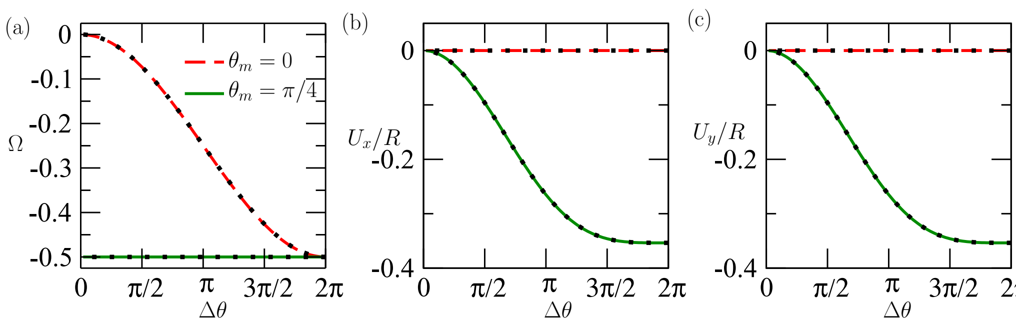

FIG. 4. Rigid-body motion vs $\Delta\theta$. Comparing the analytical values of (a) Ω, (b) U_x, and (c) U_y, given in Eqs. (38)–(40), respectively (full/dashed line), with computed values of the 2D SBT (black circles). The computations are for $\theta_m = 0$ (red-dashed line) and $\theta_m = \pi/4$ (green solid line) and for $\boldsymbol{x}_m = 0$ and $R = 2/\Delta\theta$. In simulations, $N = 200$ discretization points were used.

The coefficients A and B depend on the computation of $S_{ij}(\theta_m)$ evaluated in the particle frame and on the cross-sectional area of the particle $\mathcal{A} \sim a^2k$ by [47]

$$\frac{A}{\dot{\gamma}\eta\mathcal{A}} = \frac{S_{XX}(\pi/4) - S_{YY}(\pi/4)}{4} - \frac{S_{XY}(0)}{2}, \quad \frac{B}{\dot{\gamma}\eta\mathcal{A}} = S_{XY}(0). \tag{52}$$

The terms $S_{XX}(\pi/4) - S_{YY}(\pi/4)$ and $S_{XY}(0)$ can be rewritten as a line integral over X by [47]

$$\begin{aligned} S_{XX}(\pi/4) - S_{YY}(\pi/4) &= 2a^2 \int_{-1}^{1} X[\bar{f}_X + \partial_X(kh\Delta f_Y)]\mathrm{d}X \\ &= 2a^2 \int_{-1}^{1} XQ\mathrm{d}X, \quad Q = \bar{f}_X + \partial_X(kh\Delta f_Y) \end{aligned} \tag{53}$$

and

$$S_{XY}(0) = a^2 \int_{-1}^{1} [\bar{f}_Y X + \Delta f_X kh]\mathrm{d}X. \tag{54}$$

In these integral equations, $\bar{\boldsymbol{f}}$ and $\Delta\boldsymbol{f}$ are evaluated over the particle at the orientation $\theta_m = \pi/4$ in (53), and for $\theta_m = 0$ in (54). Similarly, the torque, evaluated in the particle frame, is

$$T(\theta_m) = 2a^2 \int_{-1}^{1} [\bar{f}_Y X - \Delta f_X kh]\mathrm{d}X, \tag{55}$$

where $\bar{f}_Y$ and Δf_X are computed over the particle when fixed at the orientation θ_m.

Analytical predictions for $\boldsymbol{u}^{\mathrm{rg}}$, A, and B exist for $k \ll 1$. For example, for a particle with an elliptical cross-section of aspect ratio k, Jeffery's theory predicts [48,49]

$$\Omega(\theta_m) = -\frac{\dot{\gamma}}{k^2+1}(k^2\cos^2\theta_m + \sin^2\theta_m). \tag{56}$$

The coefficients A and B can be computed from the analytical results of Sherwood *et al.* [50]. This result gives, for an infinitesimally slender two-dimensional particle [47],

$$A = \frac{\pi}{4\mathcal{A}} + \frac{1}{2}, \quad B = 1. \tag{57}$$

We will show that the analytical predictions for Ω, A, and B can be reproduced from the 2D SBT.

A. Leading-order 2D SBT

To compute $\boldsymbol{u}^{\mathrm{rg}}$, α, and β, it is convenient to write the "simplified" 2D SBT equation, given in (37), in the body frame. Projecting (37) in the direction $\hat{\boldsymbol{e}}_X$ gives, for a point $X_1 \in X$,

$$-\frac{1}{2\pi\eta}\int_{-1}^{1} \bar{f}_X(-\ln|X - X_1| + 2)\mathrm{d}X = -\dot{\gamma}X_1\sin\theta_m\cos\theta_m \tag{58}$$

and in the direction $\hat{\boldsymbol{e}}_Y$ gives

$$-\frac{1}{2\pi\eta}\int_{-1}^{1} \bar{f}_Y(-\ln|X - X_1|)\mathrm{d}X = +(\dot{\gamma}\sin^2\theta_m + \Omega(\theta_m))X_1. \tag{59}$$

Here, we have taken the center of the particle to be at the origin. At leading order in slenderness, $Q = \bar{f}_X$ in (53). The value of Q is computed by solving (58) for $\bar{f}_X$ when $\theta = \pi/4$. The result, which has been computed in Ref. [47], is

$$S_{XX}(\pi/4) - S_{YY}(\pi/4) = \dot{\gamma}\eta a^2\pi. \tag{60}$$

Solving Eq. (59) for $\theta_m = 0$, along with the constraint $T = 0$ in (55), gives [47]

$$\bar{f}_Y = 0, \quad \Omega(\theta_m) = -\dot{\gamma}\sin^2\theta_m. \tag{61}$$

The prediction of $\Omega(\theta_m)$ agrees exactly with the analytical value given in (40) for a flat sheet of vanishing thickness. This angular velocity is equal to zero for $\theta_m = 0$; a sheet of vanishing thickness always reorients to align indefinitely in the flow direction without rotating in time. For $k \ll 1$, (61) compares exactly to (56) up to $O(k)$, provided $k \ll |\theta_m|$. For $\theta_m = 0$, (56) predicts $\Omega(0) \approx \dot{\gamma} k^2$, which is beyond the asymptotic order at which our 2D SBT has been evaluated. Evaluating $O(k^2)$ terms is achievable; see, for example, Ref. [38] for a slender filament. However, as stated in our formulation, the effects of the edges can be significant at this order [33], and thus an accurate expansion at $O(k^2)$, for a slender particle of arbitrary shape, will depend in general on resolving the surface traction $\boldsymbol{f}$ at the edges [29,33,35].

Using the value of $\bar{f}_Y = 0$ in (61) to evaluate $S_{XY}(0)$ yields a prediction of $S_{XY}(0) = 0$, to leading order in k, and thus $B = 0$ in (52). But this result does not agree with the analytical value given in (57). We will show that predicting B instead requires evaluating the 2D SBT up to $O(k)$, which is given in Eqs. (35) and (36).

B. Next-order 2D SBT

To the next order in k, the 2D SBT corresponds to solving the following four coupled equations for a point $X_1 \in X$. Projecting (35) in the direction $\hat{\boldsymbol{e}}_X$ gives

$$-\frac{1}{4\pi\eta}\bar{\mathcal{G}}_X^{\text{out}} = -\dot{\gamma} X_1 \sin\theta_m \cos\theta_m \tag{62}$$

and in the direction $\hat{\boldsymbol{e}}_Y$ gives

$$-\frac{1}{4\pi\eta}\bar{\mathcal{G}}_Y^{\text{out}} = (\dot{\gamma}\sin^2\theta_m + \Omega(\theta_m))X_1. \tag{63}$$

Projecting (36) in the direction $\hat{\boldsymbol{e}}_X$ gives, for a point $X_1 \in X$,

$$-\frac{1}{4\pi\eta}\big(\Delta\mathcal{G}_X^{\text{out}} + 4\pi k h(s_1)\Delta f_X(s_1)\big) = -kh(\dot{\gamma}\cos^2\theta_m + \Omega(\theta_m)) \tag{64}$$

and in the direction $\hat{\boldsymbol{e}}_Y$ gives

$$-\frac{1}{4\pi\eta}\Delta\mathcal{G}_Y^{\text{out}} = \dot{\gamma} kh \sin\phi\cos\phi. \tag{65}$$

From the linearity of the Stokes equations, a linear flow field can be decomposed into a shear or extensional component [51]. Equations (63) and (64) are equations for $\bar{f}_Y$ and Δf_X originating from the shear component of the flow $\dot{\gamma}(-kh\cos^2(\theta_m), X_1\sin^2(\theta_m))$, and Eqs. (62) and (65) are equations for $\bar{f}_X$ and Δf_Y originating from the extensional component of the flow $\dot{\gamma}\cos\theta_m\sin\theta_m(-X_1, kh)$.

Equations (63) and (64), along with the condition $T = 0$, provide a closed system of equations for $\bar{f}_Y$, Δf_X, and Ω. This system of equations has been computed analytically in Ref. [47]. The result is

$$\Delta f_X \approx \dot{\gamma}\eta, \quad \bar{f}_Y \approx k\partial_X(h\Delta f_X), \quad \Omega(\theta_m) = -\dot{\gamma}\sin^2\theta_m. \tag{66}$$

The computed value of Ω is identical to that obtained in Eq. (61). Inserting (66) into (54), and evaluating analytically the integrals, gives [47]

$$S_{XY}(0) = \eta\dot{\gamma}\mathcal{A}. \tag{67}$$

Equations (62) and (65) have also been computed analytically for $\bar{f}_X$ and Δf_Y in Ref. [47] using a series expansion for $\bar{f}_X$ and Δf_Y in s. Using these values to compute $S_{XX}(\pi/4) - S_{YY}(\pi/4)$, it is found that [47]

$$S_{XX}(\pi/4) - S_{YY}(\pi/4) = \dot{\gamma}\eta a^2\pi. \tag{68}$$

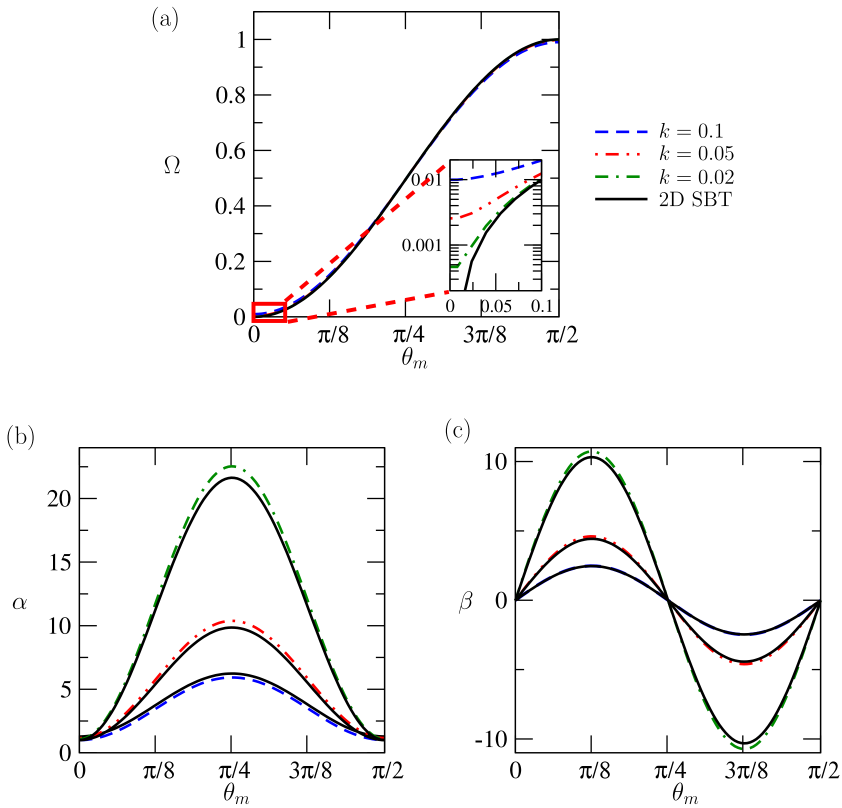

FIG. 5. Comparison of (a) Ω, (b) α, and (c) β vs θ_m. (a) Comparison between the 2D SBT computation of Ω (61) (solid black line) with Eq. (56) for selected values of k (dashed/dashed-dotted lines); (b),(c) comparison of BI computations of α and β (dashed/dashed-dotted line) with the 2D SBT computations (solid black line) for selected k.

Substituting (67) and (68) into (52), the coefficients A and B are

$$B \approx 1, \quad A \approx \frac{\pi a^2}{4\mathcal{A}} - \frac{1}{2}, \tag{69}$$

in agreement with the analytical prediction given in (57).

To demonstrate the accuracy of our results, obtained from the 2D SBT, in Fig. 5(a) we compare Ω for computed values from Jeffery's theory (56) and the STB theory (61) for selected k. The plot shows good agreement for Ω, except when $\theta_m \ll k$. In this regime, the 2D STB theory is unable to predict the $O(k^2)$ leading term in Ω (inset). We also compare computed values of α and β versus θ_m between 2D SBT computations and numerical boundary integral computations (BI) for selected k, Figs. 5(b) and 5(c). For the BI computations, we use the numerical code in Ref. [47] to obtain α and β for a particle whose cross-section has rounded edges. The particle's cross-section consists of a rectangular central part of half-length equal to $1-k$ and two semicircular edges of radius k. The predictions of A and B from the 2D SBT computations (69) are $A = 2.46,\ 4.27$ and $A = 10.3$ and $B = 1$ for $k = 0.1,\ 0.05$, and 0.02, respectively, compared to $A = 2.47,\ 4.46$, and 10.7, and $B = 1.28,\ 1.17$, and 1.08, respectively, from BI computations. These values of A and B are used to compute α and β from (52). The plots in Figs. 5(b) and 5(c) show a good comparison between values of α and β from 2D SBT computations and the BI computations. When $\theta_m \to 0$ or $\pi/2$, the contribution within brackets in α vanishes and therefore $\alpha \approx B$. The error between the 2D

SBT and BI computations is of order $O(k)$ for this orientation of the particle, corresponding to the order of validity of the 2D SBT's computation of B. Otherwise, for all other particle orientations, $\alpha \approx A(1-\cos 4\theta_m)$. Since the leading term in the 2D SBT computation of A scales like $O(1/k)$, the error between the 2D SBT and BI computations for both α and β is of $O(1)$ for all particle orientations excluding the orientations close to the limits $\theta_m = 0$ or $\pi/2$. For this reason, the error between computed values from 2D SBT and BI is greatest for $\theta_m = \pi/4$ in Figs. 5(b) and 5(c).

C. Evaluating the accuracy of 2D SBT for particles in a linear flow field

An analytical characterization for the rotational orbits of axisymmetric particles or, in the case of two-dimensional flow, of particles with two lines of symmetry is given by Bretherton [49]. Here, we will show how Bretherton's theory can be used to determine the accuracy of our 2D SBT model. Bretherton's theory relies on a single parameter, k_e, defined as the square root of the ratio between the torque acting on the particle when its major axis is held fixed parallel, $T(0)$, or perpendicular, $T(\pi/2)$, to the flow direction,

$$k_e = \sqrt{T(0)/T(\pi/2)}. \tag{70}$$

The computed value of k_e can be used to validate the range of particle orientations and degree of particle curvature at which the 2D SBT theory accurately approximates the particle's rotational motion. According to Bretherton, the particle's minimum angular velocity is given by $\Omega^{\min} = -\dot{\gamma} k_e/(1+k_e^2) \approx -\dot{\gamma} k_e$. For the approximation $\Omega^{\min} \approx -\dot{\gamma} k_e$, we have assumed $|k_e| \ll 1$ for slender two-dimensional particles and that the minimization of the angular velocity occurs when the particle's centerline is straight and the particle's major axis is aligned with the flow direction. The value of $\Omega^{\min}$ depends either on the edge contributions or on higher-order expansions of our 2D SBT with respect to the particle's slenderness parameter. If the angular velocity of a torque-free particle obtained from 2D SBT is greater than $\Omega^{\min}$, then it indicates that the 2D SBT is indeed accurate in predicting the rotational motion of the particle.

The computational value of $|k_e| \ll 1$ depends strongly on the particle's geometric aspect ratio, cross-sectional shape (e.g., elliptical, a pointed diamond, or rectangular) and surface boundary condition (e.g., no-slip or Navier slip) [33,34]. Existing analytical or computational values of k_e can be used to estimate the accuracy of our 2D SBT model. For example, for the case of a no-slip particle, $k_e \propto [k, k^{3/4}]$ [33]. The relationship $k_e \propto k$ is obtained for particles with an elliptical cross-section or tapered edges [33], while $k_e \propto k^{3/4}$ applies to particles with a rectangular-shaped cross-section [29,33]. Since the value of $\Omega^{\min}$ approximately lies between $-\dot{\gamma} k$ and $-\dot{\gamma} k^{3/4}$, $\Omega^{\min}$ is small for $k \ll 1$. Thus the 2D SBT fails only for a small range of particle orientations close to the flow direction and for small particle curvature, as demonstrated in Fig. 5(a) for a flat filament.

VI. VALIDITY OF 2D SBT: TAYLOR'S SHEET

The 2D SBT can be used to obtain solutions for slender active particles. As an example, we compare the swimming speed of a propagating active sheet, known as a Taylor sheet, between computational values obtained from the 2D SBT and analytical values. The Taylor sheet [27,28] is a classical model of a swimming sheet at a low Reynolds number (see Fig. 6). It consists of a waving sheet, infinite in the $\hat{\boldsymbol{e}}_x$ and $\hat{\boldsymbol{e}}_z$ directions and with zero thickness, perturbed by a wave propagating in the $\hat{\boldsymbol{e}}_x$ direction. The vectors $\hat{\boldsymbol{e}}_x$, $\hat{\boldsymbol{e}}_y$, and $\hat{\boldsymbol{e}}_z$ correspond to orthogonal unit vectors. The wave speed propagating on the sheet is $V^* = \omega^*/k^*$, where ω^* is the frequency and k^* is the wave number [11]. Here the superscript $[*]^*$ represents dimensional units.

The material point on the sheet, denoted by (x^*, y^*), follows a prescribed waving motion. Assuming the material point on the sheet undergoes a transverse displacement only, the waving motion is

$$y^* = B^* \sin(k^* x^* - \omega^* t^*). \tag{71}$$

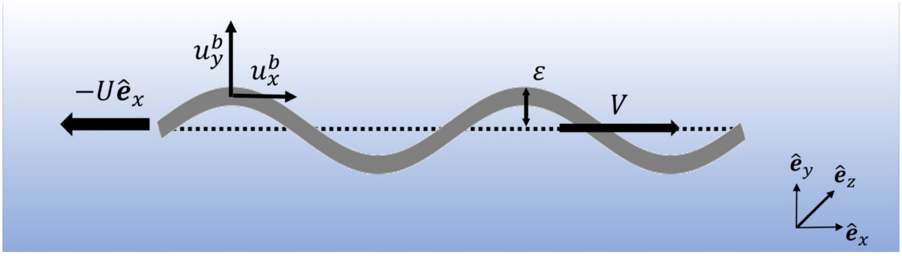

FIG. 6. Sketch of a Taylor sheet perturbed by a wave propagating in the positive $\hat{\boldsymbol{e}}_x$ direction with amplitude ε and velocity V.

The nondimensional equation, in terms of the nondimensional variables $x = x^*k^*$, $t = t^*\omega^*$ and the nondimensional amplitude $\varepsilon = B^*k^*$, reads

$$y = \varepsilon \sin(x - t). \tag{72}$$

Assuming the sheet to be force-free, the transverse displacement causes the sheet to translate with a swimming velocity $-U\hat{\boldsymbol{e}}_x$. In a frame attached to the particle, the wave propagating in the sheet induces a disturbance velocity $U\hat{\boldsymbol{e}}_x$ in the fluid. In the laboratory frame, this corresponds to the sheet moving with a velocity $-U\hat{\boldsymbol{e}}_x$ in a fluid at rest.

The no-slip condition is imposed on the surface of the sheet, as well as the inextensibility of the sheet. In a frame of reference moving at the sheet speed $-U$, the last constraint leads to the boundary condition for the deformation velocity of the surface $\boldsymbol{u}^{\mathrm{b}} = (u_x^b, u_y^b)$ [28],

$$u_x^b = 1 - q\cos\theta, \quad u_y^b = -q\sin\theta, \tag{73}$$

where

$$q = \frac{1}{2\pi}\int_0^{2\pi}(1 + \varepsilon^2\cos^2 z)^{1/2}dz \tag{74}$$

is the material velocity in the moving frame, $z = x - t$, and $\tan\theta = \partial y/\partial z$.

The velocity U has been solved analytically up to fourth order in ε in Ref. [27], and to infinite order in ε in Ref. [28], in which an algorithm is also given to solve U analytically for moderate and large ε. A list of the coefficients of the series expansion of U is provided in Ref. [28] up to $O(\varepsilon^{500})$. The first few terms of the sequence are, up to five decimal points,

$$U = (1/2)\,\varepsilon^2 - 0.593\,75\,\varepsilon^3 + 0.640\,63\,\varepsilon^4 + O(\epsilon^5). \tag{75}$$

A. 2D SBT evaluation for a Taylor sheet

To compute U from the 2D SBT, we use (37) with $\bar{\boldsymbol{u}}^{rg} = -U\hat{\boldsymbol{e}}_x$ and $\bar{\boldsymbol{u}}^b = \boldsymbol{u}^b$, where $\boldsymbol{u}^b$ is given in (73). The 2D SBT is thus

$$-U\hat{\boldsymbol{e}}_x + \boldsymbol{u}^b(\boldsymbol{x_0}) = -\frac{1}{2\pi\eta}\int_{\mathcal{L}}[\bar{\boldsymbol{f}}\cdot\boldsymbol{G}(s, s_1)]\mathrm{d}L(s), \tag{76}$$

where the line integral is taken over the line corresponding to $\boldsymbol{x}_0$. Equation (76) along with the condition of zero force, can be solved for the unknown tractions $\bar{\boldsymbol{f}}$ and the velocity U. We will solve U assuming the length of the sheet is of infinite or finite extent in the $\hat{\boldsymbol{e}}_x$ direction, corresponding to an "infinite sheet" or a "finite sheet," respectively.

1. Infinite extent

To solve the problem for an infinite sheet, a periodic Green's function [28,30,52] can be used in the 2D SBT. For this case, the tensor $\boldsymbol{G}(s, s_1)$ in Eq. (76) corresponds, for $x \in [-\pi, \pi]$, to

$$\boldsymbol{G}(s, s_1) = \begin{pmatrix} -A - \hat{y}\partial A_y + 1 & \hat{y}\partial A_x \\ \hat{y}\partial A_x & -A + \hat{y}\partial A_y \end{pmatrix}, \tag{77}$$

where

$$A = \tfrac{1}{2}\ln(2\cosh\hat{y} - 2\cos\hat{x}), \tag{78}$$

∂A_x, ∂A_y are the derivatives of A with respect to x and y, and $\hat{x} = x - x_0$, $\hat{y} = y - y_0$.

2. Finite extent

When the sheet is of finite extent, U is found by solving numerically Eq. (76) for a sheet of length $x \in [-p\pi, p\pi]$, using the free-space Green's functions with corresponding tensors given in (7). The parameter p defines the number of spatial periods.

3. Numerical procedure

The numerical procedures to solve Eq. (76) for the infinite-extent case and the finite-extent case are similar. In both cases, the surface of the sheet is discretized in straight-line elements of equal size. The tractions $\bar{\boldsymbol{f}}$ are discretized as a piecewise continuous function at the midpoint of each straight-line element. The 2D SBT equation, given in (76), is then evaluated numerically over each line element using a 20-point Gauss-Legendre quadrature either for the periodic Green's function or for the free-space Green's function for $x \in [-p\pi, p\pi]$. If the element is singular, an alternative method is used to evaluate the element. For the finite-sheet case, this corresponds to subtracting the logarithmic singularity and integrating it analytically [28,30]. The remainder of the integral is regular and is evaluated using the same procedure for a regular element. For the infinite-sheet case, it can be shown that the periodic Green's function approaches the free-space Green's function as the singular point is approached [30]. Therefore, the singular element can likewise be evaluated by subtracting the logarithmic singularity and integrating it analytically [28,52]. The discretized equations form a linear system for the discrete traction vectors and for U, and they require the addition of a further equation to be solved. This equation corresponds to the free-force equation for the tractions in the x direction. The system is then solved by Gaussian elimination to obtain the discrete traction vectors and U.

For the infinite case, U is constant with time. For the finite case, however, U varies with time and the average swimming speed needs to be calculated. The swimming speed is calculated for evenly spaced values of $t \in [0, 2\pi]$, and then averaged in time to find the average swimming speed $\langle U \rangle$. Denoting the discrete-time elements by t_k for $k = 1 : N_2$, the time-averaged speed was obtained by using a three-point polynomial to approximate the curve between each t_k and t_{k+1} element [53], and then integrating the polynomial to find the area over each element.

In our computations in the infinite-sheet case, we set the number of discretization elements as $N = 50$ to ensure numerical convergence. This corresponds to discretizing a single spatial period, with $x \in [-\pi, \pi]$, in 50 elements. Consequently, for the finite-sheet case, the number of discretization points has been scaled with the number of spatial periods, by imposing $N = 50p$. Additionally, in the finite-sheet case, the time step for the calculation of the average velocity has been set to $\Delta t = 2\pi/20$.

B. Comparing 2D SBT computations with analytical computations of *U*

We first applied the 2D SBT equation to the infinite-sheet case to obtain the swimming speed and compare it with the series expansion (75) given in Sauzade *et al.* [28]. The results are shown in Figure 7(a) and show a great accordance between the series solution and the 2D SBT data,

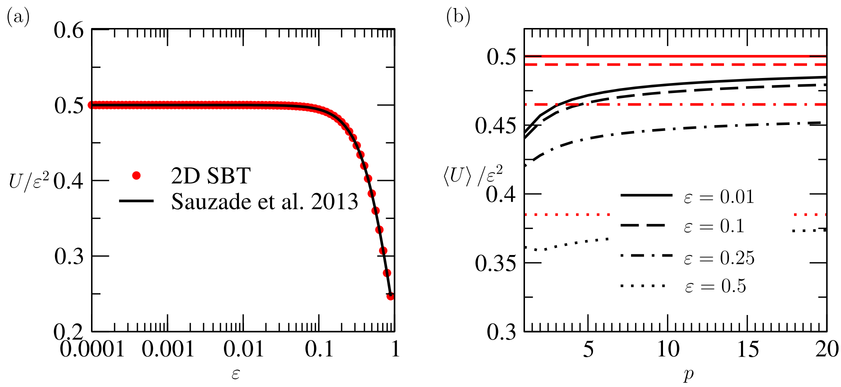

FIG. 7. Average swimming speed for different amplitudes. (a) U/ε^2 vs ε, comparing 2D SBT computations for an infinite-sheet (red circles) and the analytical series expansion from Sauzade *et al.* [28] up to $O(\varepsilon^{500})$ (black solid line). (b) $\langle U\rangle/\varepsilon^2$ vs p, comparing 2D SBT computations for a sheet of finite spatial periods (black curved lines) with the infinite sheet computations (red horizontal lines) and for selected values of the normalized wave amplitude ε.

supporting the validity of our model. In Sauzade *et al.*, the series expansion had been validated with boundary integrals simulations including both the $\mathcal{G}$ and the $\mathcal{K}$ kernel in (4). Our results confirm that the $\mathcal{K}$ kernel is indeed subdominant for ultrathin particles.

We then compared the results obtained for the infinite sheet with those from 2D SBT applied to a sheet of finite length. We calculated the average velocity and repeated the simulation for different values of the parameter p, i.e. for increasing sheet length. The comparison between the swimming velocity in the case of an infinite and finite sheet is shown in Fig. 7(b), for selected values of the normalized wave amplitude. The swimming speed of a finite sheet appears to converge to the speed of an infinite sheet for an increasing number of spatial periods.

The difference between the results for the finite- and infinite-sheet cases can be explained by considering the behavior of the traction along the particle length. In the case of the infinite sheet, there are no free edges by definition, therefore the traction does not diverge at any point of the sheet. In the finite-sheet case, the tractions are expected to diverge near and on the edges. The x and y components of the traction are plotted in Figs. 8(a) and 8(b), respectively, for the infinite-sheet case (where a periodic Green's function is used) and for selected values of the spatial period in the case of a finite sheet (obtained with the free space Green's function). For a finite sheet (red dashed, dashed-dotted, and dotted lines), the traction shows the expected divergent behavior near and on the edges.

The insets in Fig. 8 show the central region of the sheet. In this region, far from the edges, the traction on a finite sheet converges to the traction on an infinite sheet for increasing the value of the spatial period p.

The divergent behavior on the edges does not play a dominant role in the dynamics and the average swimming speed appears to converge, although slowly, as shown in Fig. 7(b). The result for larger values of p is plotted in Fig. 9 for the amplitude $\varepsilon = 0.01$, where the velocity is expected to converge to 0.5.

VII. CONCLUSION AND DISCUSSION

This article presents a slender body theory for ultrathin platelike particles in two-dimensional viscous flow (2D SBT). The 2D SBT is derived by expanding the boundary integral formulation of incompressible Stokes flow, which provides an integral relation for the velocity and traction around the two-dimensional boundary of the particle, to leading order in the particle's slenderness k. When the particle is sufficiently bent, the 2D SBT simplifies to a line integral of point forces over the

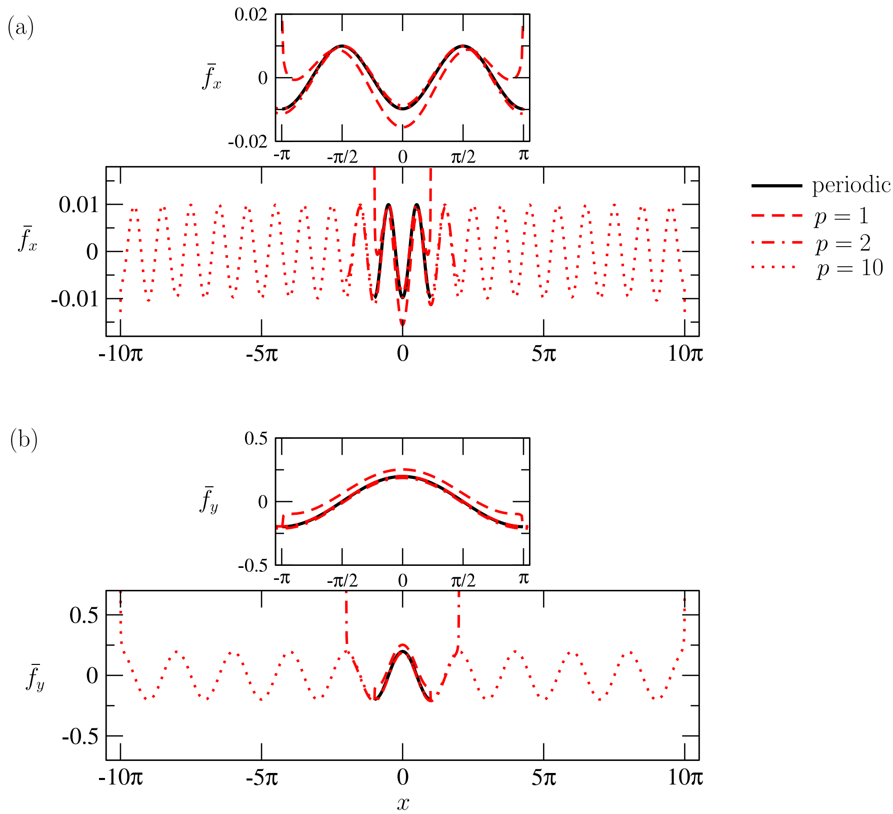

FIG. 8. Hydrodynamic traction distributions obtained with 2D SBT. Comparing (a) $\bar{f}_x$ vs x and (b) $\bar{f}_y$ vs x for an infinite sheet (periodic Green's function, black solid line) and a finite sheet for selected p (red dashed, dashed-dotted, and dotted lines). The amplitude is $\varepsilon = 0.01$.

particle's centerline $\boldsymbol{x}_0$. This formulation is similar to what was proposed in [23–25] up to a factor of 2: in our model, the strength of the point force is twice the suggested force in Refs. [23–25] due to the point force contributions from both the top and bottom boundary.

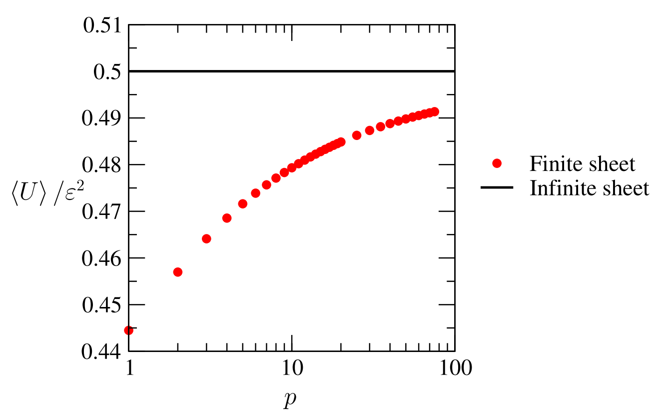

FIG. 9. Average swimming speed vs p. Comparing 2D SBT computations of $\langle U \rangle$ for finite p (red circles) with computational values for the periodic 2D SBT (solid black line). The wave amplitude is $\varepsilon = 0.01$.

We validated our model for three test cases for which analytical solutions exist, namely (i) the motion of a curved arc in shear flow, (ii) the instantaneous stresslet tensor and rigid-body motion for an ultrathin plate in external shear, and (iii) the propagating speed of a Taylor's sheet. We found that for cases (i) and (iii), a simplified version of the 2D SBT equation given in (37), which ignores $O(k)$ corrections, was sufficiently accurate for obtaining values in good agreement with the analytical results. For case (ii), the full version of the 2D SBT equation, up to $O(k)$, given in (35) and (36), is required to reproduce the analytical results to good accuracy.

Our model is designed for two-dimensional flow. Understanding the behavior of elastic ultrathin plates (active or passive) in viscous flow starts with two-dimensional flow analysis. Two-dimensional domains can offer valuable insights into the flow and rheology of particles [6–8], while allowing for computational convenience. Additionally, in certain cases, a physical reasoning for a two-dimensional approximation can be justified. For example, in the coalescence of elastic blisters [54] or the peeling of an elastic sheet [55], a quasi-two-dimensional dynamics is often observed for a particle whose depth is comparable to its length. Another example is a platelike graphene particle in shear. It has been shown from fully three-dimensional molecular-dynamics simulations that the graphene particle can align indefinitely in shear flow due to the presence of hydrodynamic slip, rather than tumble as assumed for a classical no-slip particle [20]. Two-dimensional continuum simulations have been shown to provide good agreement with the dynamics and effective viscosity of the graphene particles for this case [20].

The 2D SBT presented in this paper is highly accurate for predicting the flow and rheology of ultrathin platelike particles in viscous flow. Our model can be adapted to different geometries by using different Green's functions that satisfy the domain boundary condition, such as the one-periodic Green's function that we used in case (iii). This flexibility reduces computational costs for various domains, such as those bounded by a wall or in channel flow [30]. When dealing with multiple plates, it is only necessary to evaluate a nonlocal 1D line integral over the central line of each particle and not over the entire particle boundary. This simplification further reduces the computational cost, allowing for the simulation of systems with multiple particles.

ACKNOWLEDGMENTS

C.K. and G.S. would like to thank Eric Lauga and Gwynn Elfring for their helpful discussion on the Taylor sheet. Funding from the Royal Society Dorothy Hodgkin fellowship, Grant No. G119482, is gratefully acknowledged (C.K.).

DATA AVAILABILITY

The data are available in the GitHub repository [56] or on request.

---

[1] S. L. Tawari, D. L. Koch, and C. Cohen, Electrical double-layer effects on the Brownian diffusivity and aggregation rate of Laponite clay particles, J. Colloid Interface Sci. **240**, 54 (2001).

[2] P. C. Rijo and F. J. Galindo-Rosales, Rheological behavior of molybdenum disulfide (MoS2) inks under electric fields: influence of concentration and voltage, arXiv:2408.11506.

[3] C. O'Mahony, E. Ul Haq, C. Silien, and S. A. M. Tofail, Rheological issues in carbon-based inks for additive manufacturing, Micromachines **10**, 99 (2019).

[4] C. Vaquero-Stainer, T. Miara, A. Juel, D. Pihler-Puzović, and M. Heil, U-shaped disks in stokes flow: Chiral sedimentation of a non-chiral particle, J. Fluid Mech. **999**, A71 (2024).

[5] C. Lin, S. Wang, V. Narsimhan, and S. Kim, Surface discretization considerations for the boundary-element method applied to three-dimensional ellipsoidal particles in Stokes flow, Phys. Fluids **33**, 113106 (2021).

[6] C. Pozrikidis, Dynamic simulation of the flow of suspensions of two-dimensional particles with arbitrary shapes, Eng. Anal. Boundary Elem. **25**, 19 (2001).
[7] C. Pozrikidis, Orientation statistics and effective viscosity of suspensions of elongated particles in simple shear flow, Eur. J. Mech. B **24**, 125 (2005).
[8] C. Kamal and L. Botto, Flow and rheology of suspensions of two-dimensional cylindrical or anisotropic particles with navier slip, Phys. Rev. Fluids **9**, 074102 (2024).
[9] R. E. Johnson, An improved slender-body theory for Stokes flow, J. Fluid Mech. **99**, 411 (1980).
[10] J. Lighthill, Flagellar hydrodynamics, SIAM Rev. **18**, 161 (1976).
[11] E. Lauga, *The Fluid Dynamics of Cell Motility* (Cambridge University Press, Cambridge, 2020), Vol. 62.
[12] L. Koens and E. Lauga, Slender-ribbon theory, Phys. Fluids **28**, 013101 (2016).
[13] L. Koens, Tubular-body theory for viscous flows, Phys. Rev. Fluids **7**, 034101 (2022).
[14] C. Brennen and H. Winet, Fluid mechanics of propulsion by cilia and flagella, Annu. Rev. Fluid Mech. **9**, 339 (1977).
[15] O. du Roure, A. Lindner, E. N. Nazockdast, and M. J. Shelley, Dynamics of flexible fibers in viscous flows and fluids, Annu. Rev. Fluid Mech. **51**, 539 (2019).
[16] J. F. Brady, G. Bossis *et al.*, Stokesian dynamics, Annu. Rev. Fluid Mech. **20**, 111 (1988).
[17] Q. Meng and J. J. L. Higdon, Large scale dynamic simulation of platelike particle suspensions. Part I: Non-Brownian simulation, J. Rheol. **52**, 1 (2008).
[18] K. S. Silmore, M. S. Strano, and J. W. Swan, Buckling, crumpling, and tumbling of semiflexible sheets in simple shear flow, Soft Matter **17**, 4707 (2021).
[19] J. Guo, Q. Zhou, and R. C.-K. Wong, Effects of volume fraction and particle shape on the rheological properties of oblate spheroid suspensions, Phys. Fluids **33**, 081703 (2021).
[20] S. Gravelle, C. Kamal, and L. Botto, Violations of jeffery's theory in the dynamics of nanographene in shear flow, Phys. Rev. Fluids **6**, 034303 (2021).
[21] Y. Yu and M. D. Graham, Coil-stretch-like transition of elastic sheets in extensional flows, Soft Matter **17**, 543 (2021).
[22] Y. Yu and M. D. Graham, Free-space and near-wall dynamics of a flexible sheet sedimenting in stokes flow, Phys. Rev. Fluids **9**, 054104 (2024).
[23] G. Salussolia, C. Kamal, J. Stafford, N. Pugno, and L. Botto, Simulation of interacting elastic sheets in shear flow: Insights into buckling, sliding, and reassembly of graphene nanosheets in sheared liquids, Phys. Fluids **34**, 053311 (2022).
[24] H. Perrin, H. Li, and L. Botto, Hydrodynamic interactions change the buckling threshold of parallel flexible sheets in shear flow, Phys. Rev. Fluids **8**, 124103 (2023).
[25] S. D. Olson and L. J. Fauci, Hydrodynamic interactions of sheets vs filaments: Synchronization, attraction, and alignment, Phys. Fluids **27**, 121901 (2015).
[26] D. Crowdy, Flipping and scooping of curved 2D rigid fibers in simple shear: The Jeffery equations, Phys. Fluids **28**, 053105 (2016).
[27] G. I. Taylor, Analysis of the swimming of microscopic organisms, Proc. R. Soc. Lond. Ser. A **209**, 447 (1951).
[28] M. Sauzade, G. J. Elfring, and E. Lauga, Taylor's swimming sheet: Analysis and improvement of the perturbation series, Physica D **240**, 1567 (2011).
[29] C. Kamal, S. Gravelle, and L. Botto, Effect of hydrodynamic slip on the rotational dynamics of a thin Brownian platelet in shear flow, J. Fluid Mech. **919**, A1 (2021).
[30] C. Pozrikidis, *Boundary Integral and Singularity Methods for Linearized Viscous Flow* (Cambridge University Press, Cambridge, 1992).
[31] L. Koens and E. Lauga, The boundary integral formulation of stokes flows includes slender-body theory, J. Fluid Mech. **850**, R1 (2018).
[32] E. J. Hinch, *Perturbation Methods* (Cambridge University Press, Cambridge, 1991).
[33] V. Singh, D. L. Koch, G. Subramanian, and A. D. Stroock, Rotational motion of a thin axisymmetric disk in a low Reynolds number linear flow, Phys. Fluids **26**, 033303 (2014).
[34] C. Kamal, S. Gravelle, and L. Botto, Hydrodynamic slip can align thin nanoplatelets in shear flow, Nat. Commun. **11**, 2425 (2020).

[35] C. Kamal, S. Gravelle, and L. Botto, Alignment of a flexible platelike particle in shear flow: Effect of surface slip and edges, Phys. Rev. Fluids **6**, 084102 (2021).

[36] S. H. Smith, Stokes flow past slits and holes, Int. J. Multiphase Flow **13**, 219 (1987).

[37] D. Crowdy and O. Samson, Stokes flows past gaps in a wall, Proc. R. Soc. A **466**, 2727 (2010).

[38] R. G. Cox, The motion of long slender bodies in a viscous fluid. Part 2. Shear flow, J. Fluid Mech. **45**, 625 (1971).

[39] W. R. Dean and P. E. Montagnon, On the steady motion of viscous liquid in a corner, *Mathematical Proceedings of the Cambridge Philosophical Society* (Cambridge University Press, Cambridge, 1949), Vol. 45, pp. 389–394.

[40] H. K. Moffatt, Viscous and resistive eddies near a sharp corner, J. Fluid Mech. **18**, 1 (1964).

[41] H. Masoud and H. A. Stone, The reciprocal theorem in fluid dynamics and transport phenomena, J. Fluid Mech. **879**, P1 (2019).

[42] E. Lauga, M. P. Brenner, and H. A. Stone, Microfluidics: The no-slip boundary condition, in *Springer Handbook of Experimental Fluid Mechanics*, edited by C. Tropea, J. F. Foss, and A. Yarin (Springer, Berlin, Heidelberg, 2008), p. 1219.

[43] C. Pozrikidis, *A Practical Guide to Boundary Element Methods with the Software Library BEMLIB* (CRC, Boca Raton, FL, 2002).

[44] J. J. L. Higdon, Stokes flow in arbitrary two-dimensional domains: shear flow over ridges and cavities, J. Fluid Mech. **159**, 195 (1985).

[45] L. G. Leal and E. J. Hinch, The effect of weak Brownian rotations on particles in shear flow, J. Fluid Mech. **46**, 685 (1971).

[46] E. J. Hinch and L. G. Leal, The effect of Brownian motion on the rheological properties of a suspension of non-spherical particles, J. Fluid Mech. **52**, 683 (1972).

[47] C. Kamal and L. Botto, The effect of navier slip on the rheology of a dilute two-dimensional suspension of plate-like particles, J. Fluid Mech. **972**, A1 (2023).

[48] G. B. Jeffery, The motion of ellipsoidal particles immersed in a viscous fluid, Proc. R. Soc. Lond. A **102**, 161 (1922).

[49] F. P. Bretherton, The motion of rigid particles in a shear flow at low Reynolds number, J. Fluid Mech. **14**, 284 (1962).

[50] J. D. Sherwood and G. H. Meeten, The use of the vane to measure the shear modulus of linear elastic solids, J. Non-Newtonian Fluid Mech. **41**, 101 (1991).

[51] S. Kim and S. J. Karrila, *Microhydrodynamics: Principles and Selected Applications* (Butterworth-Heinemann, Boston, London, 2013).

[52] C. Pozrikidis, Creeping flow in two-dimensional channels, J. Fluid Mech. **180**, 495 (1987).

[53] W. H. Press, *Numerical Recipes, 3rd ed.: The Art of Scientific Computing* (Cambridge University Press, Cambridge, 2007).

[54] T. Sæter, C. Pedersen, J. H. Snoeijer, T. Salez, and A. Carlson, Coalescence of elastic blisters filled with a viscous fluid, Phys. Rev. Lett. **132**, 074001 (2024).

[55] A. Agrawal, S. Gravelle, C. Kamal, and L. Botto, Viscous peeling of a nanosheet, Soft Matter **18**, 3967 (2022).

[56] https://github.com/users/catherinekamal/projects/1.